PETROLOGY OF MANTLE PERIDOTITES AND INTRUSIVE MAFIC ROCKS FROM THE KERMANSHAH OPHIOLITIC COMPLEX (ZAGROS BELT, IRAN): IMPLICATIONS FOR THE GEODYNAMIC EVOLUTION OF THE NEO-TETHYAN OCEANIC BRANCH BETWEEN ARABIA AND IRAN

Khalil Allahyari*, Emilio Saccani,✉, Mohamad Pourmoafi*, Luigi Beccaluva**** and **Fariborz Masoudi***

* *Faculty of Earth Science, Shahid Beheshti University, Tehran, Iran.*
** *Dipartimento di Scienze della Terra, Università di Ferrara, Italy.*
✉ *Correspondig author, e-mail: sac@unife.it*

Keywords: *Ophiolite, peridotite, gabbro. Zagros Belt, Iran.*

ABSTRACT

The Kermanshah ophiolitic complex consists of a mélange formation, which includes dismembered ophiolitic sequences. These ophiolites are located along the Main Zagros Reverse Fault, which marks the ophiolitic suture zone between the Zagros belt and the Sanandaj-Sirjan zone. They represent the Neo-Tethyan oceanic lithosphere, which originally existed between the Arabian (to the south) and Eurasian (to the north) continental margins. The Kermanshah ophiolites were emplaced onto platform carbonate rocks, which represented the northeastern Arabian margin.

The Kermanshah ophiolitic complex is composed of various partial sequences, which are represented by: (1) mantle tectonites consisting of depleted lherzolites and both clinopyroxene- (cpx-) rich and cpx-free harzburgites; (2) a troctolite-cumulate gabbro-isotropic gabbro sequence mainly showing pegmatoid texture; (3) a wehrlite-cumulate gabbro-isotropic gabbro sequence showing foliated texture; (4) a dyke complex; (5) very scarce pillow basalts. Mantle tectonites are volumetrically predominant and tectonically overlay the gabbroic sequences. A number of conclusions may be drawn based on petrographic observations, mineral chemistry, whole-rock chemistry, and rare earth elements (REE) modelling carried out on both mantle tectonites and intrusive rock associations. (1) The Foliated Gabbro Unit has an N-MORB chemical signature and represents a portion of oceanic crust generated in a mid-ocean ridge setting from an N-MORB-type sub-oceanic mantle. (2) The Pegmatoid Gabbro Unit displays an E-MORB signature and represents a portion of oceanic crust most likely generated from a sub-oceanic mantle source enriched in light REE (LREE). A comparison with the well-studied Oman ophiolites suggests that this sequence may have formed during the early stage of oceanic spreading. (3) The depleted lherzolites present mild depletions in heavy REE (HREE) and variable depletion in LREE. REE modelling shows that they may represent a residual mantle after 15-20% removal of N-MORB melts. Some lherzolites show a moderate enrichment in La and Ce with respect to Sm, suggesting that this residual MORB mantle was subsequently trapped in a supra-subduction zone (SSZ) mantle wedge and enriched in LREE by subduction-derived fluids. (4) The depleted harzburgites present a significant depletion in incompatible elements and REE, coupled with a marked LREE enrichment with respect to medium REE. REE modelling shows that they may represent a residual mantle after 25-30% removal of boninitic-type melts in an intra-oceanic arc setting.

INTRODUCTION

The Zagros fold-and-thrust belt extends in a NW-SE direction from the Iranian-Turkish border to the Gulf of Oman (Fig. 1). This still-active belt results from the collision of the Arabian and Eurasian plates during Cenozoic times and is one of the youngest continental collision belts within the Alpine-Himalayan orogenic system (Ricou, 1976; Ricou et al., 1977). The geodynamic evolution of the Zagros Belt is mainly related to the opening and closure of the Neo-Tethys oceanic basin. A Late Permian rift episode led to the opening of the Neo-Tethyan Ocean between the Arabian and Iranian plates. The NE-dipping subduction of this oceanic branch beneath the Iranian continental margin (Berberian and King, 1981) started in the Late Jurassic (Stampfli and Borel, 2002). The obduction of the oceanic crust began in the Late Cretaceous and was accompanied by a diachronous emplacement of ophiolites onto the southern Tethyan passive margin, which occurred during Santonian in Oman and Maastrichtian in NW Zagros (Leturmy and Robin, 2010a). The two parallel domains of the Sanandaj-Sirjan metamorphic zone and Urumieh-Dokhtar magmatic arc are believed to be the result of the NE-dipping subduction of the Neo-Tethys in this area (Berberian and King, 1981). The consumption of the Neo-Tethys and the associated continental collision are recorded by the southern Iranian ophiolites (e.g., Kermanshah, Neyriz, Fig. 1), which surface along the Main Zagros Thrust Zone (Stöcklin, 1977, Berberian and King, 1981, Alavi, 1994).

Stratigraphy, tectonics, petroleum geology and geodynamics of the Zagros Belt have been extensively developed in earlier studies (Ricou, 1976; Ricou et al., 1977; Berberian and King, 1981; Dercourt et al., 1986; Sengor et al., 1988; Stampfli and Borel, 2002), as well as in recent years (e.g., Agard et al., 2005; Leturmy and Robin, 2010b). These studies provided significant information on the regional kinematics and geodynamic evolution of the Zagros area. Nonetheless, the geochemistry and petrology of the ophiolites cropping out along the Main Zagros Thrust Zone are still poorly constrained. In the Kermanshah area (Fig. 1), Desmons and Beccaluva (1983) reported the occurrence of scattered dykes with island arc tholeiitic (IAT) affinity, while Ghazi and Hassanipak (1999) described some mantle peridotites, gabbros and volcanic rocks of both IAT and alkaline within-plate basalt (WPB) affinities. Any regional geodynamic reconstruction must take account of the fundamental geochemical characteristics of the ophiolite sequences, with particular regard to: (1) their geochemistry; (2) the nature and the partial melting conditions of the mantle sources; and (3) the mutual relationship, in terms of stratigraphy and tectonics, of the different ophiolitic units. It is, in fact, commonly accepted that the different rocks or rock associations found in ophiolitic complexes are related to distinct phases of oceanic development, such as: early oceanic rifting, oceanic spreading, intra-oceanic subduction, and oceanic accretion or obduction (see the "life cycle of ophiolites" of Shervais, 2001). Therefore, ophiolites

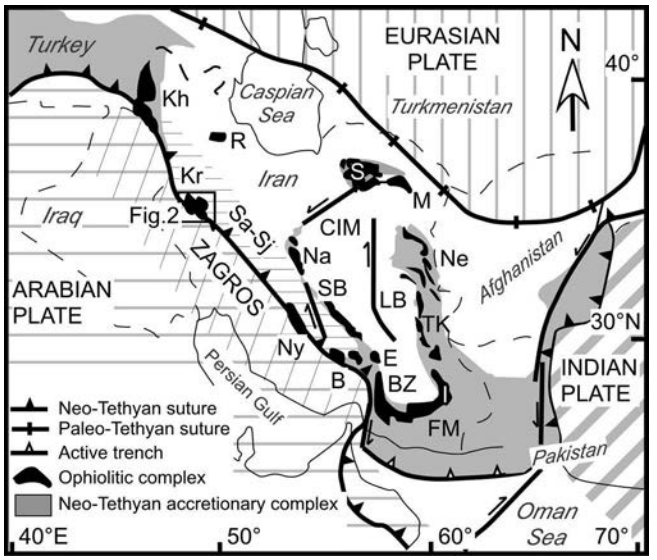

Fig. 1 - Generalized tectonic map of the Middle East. Sa-Sj: Sanandaj-Sirjan Zone; CIM: central Iran microcontinent; LB: Lut Block. The locations of the major Iranian ophiolites are also reported, B: Baft; BZ: Band-e-Zeyarat; E: Esphandagheh; FM: Fanuj-Maskutan; I: Iranshahr; Kh: Khoy; Kr: Kermanshah; M: Mashhad; Na: Nain; Ny: Neyriz; Ne: Nehbandan; R: Rasht; S: Sabzevar; SB: Shahr-Babak; TK: Tchehel Kureh. The box indicates the area expanded in Fig. 2.

commonly provide fundamental constraints on the geodynamic evolution of ancient oceanic basins and surrounding areas. For this reason, new petrological and geochemical data on the mantle tectonites and gabbroic sequences from the Kermanshah ophiolitic complex, which represents a key area of the Zagros suture belt (Fig. 1), are presented in this paper with the aim of constraining the geochemical and petrogenetic processes behind the formation and consumption of the Neo-Tethyan oceanic sector in the Iranian area. Geodynamic models for the evolution of this branch of the Neo-Tethys are available in literature (Dercourt et al., 1986; Berberian and King, 1981; Sengor et al., 1988; Stampfli and Borel, 2002; Agard et al., 2005; Robertson, 2007). Hence, the data presented in this paper will also be used for testing and developing the models already proposed for the tectonic evolution of the Iranian Neo-Tethyan Ocean.

GENERAL GEOLOGICAL SETTING AND FIELD EVIDENCE

The Kermanshah ophiolites are located along the Main Zagros Reverse Fault, which marks the ophiolitic suture zone between the Zagros Belt and the Sanandaj-Sirjan zone (Fig. 1). The Zagros Belt consists of shelf deposits (mainly limestones) of Permo-Triassic to Late Cretaceous-Paleocene age, followed by a Paleocene to Pliocene succession of various sedimentary deposits (Stöcklin, 1974; Berberian and King, 1981). The shelf deposits have been compared to those of Arabia and interpreted as representing the northeastern Arabian margin. The Zagros Belt is characterized by NW-SE-trending folds that formed after the Miocene (Stöcklin, 1968).

The Sanandaj-Sirjan zone consists of a polyphase sedimentary/metamorphic complex that forms the southern margin of the Iranian continental block (Stöcklin, 1968; 1974; Berberian and King, 1981). This zone is made of Jurassic, interbedded phyllites and metavolcanic rocks intruded by Mesozoic calc-alkaline plutons. Braud and Bellon (1974) interpreted the phyllites as backarc basin deposits, which represent a lateral variation of the Songor volcanic arc series. The metamorphic series is unconformably overlain by Barremian-Aptian limestones, which are typical of Central Iran (Stöcklin, 1968). From Middle Jurassic to Cretaceous, the Sanandaj-Sirjan zone represented an Andean-type margin with abundant calc-alkaline magmatic activity (Berberian and King, 1981). According to these authors, the calc-alkaline magmatic activity progressively shifted northwards from the Eocene to Present, leading to the formation of the Urumieh Dokhtar arc.

The suture zone along the Main Zagros Reverse Fault consists of tectonically imbricated slices of: (1) Mesozoic limestones and radiolarites; (2) ophiolitic remnants; (3) Eocene volcanic rocks and flysch. The radiolarites, and associated turbiditic limestones, strongly resemble the well-known Pichakum Formation from the Neyriz area (Ricou, 1968). In many places along the Main Zagros Reverse Fault, tightly folded radiolarite sequences may reach up to 500 m thickness and tectonically overlay the Late Cretaceous shelf limestones of the Arabian platform. In general, radiolarites range in age from Late Triassic to Cretaceous (Braud, 1970), while in the Kermanshah area, they show a Maastrichtian age (Shahidi and Nazari, 1997). The tectonic setting of formation of the radiolarites and their relationship with ophiolites are still matter of debate (e.g., Stöcklin, 1974; Agard et al., 2005). According to some authors (see Stöcklin, 1974 for a detailed review), the radiolarite-ophiolite sequence was formed in an oceanic setting, while other authors suggest that it deposited on the subsiding shelf of the Arabian margin.

The Kermanshah ophiolites (Fig. 1) are represented by an ophiolitic mélange (Stöcklin, 1974), which includes different types of ophiolitic rocks occurring as isolated and dismembered fragments (Fig. 2). These ophiolitic remnants include: (1) mantle peridotites; (2) gabbroic partial sequences; (3) a dyke complex; (4) pillow basalts. Mantle peridotites are the volumetrically most abundant ophiolitic variety (Fig. 2). They consist of mantle tectonites of lherzolitic and harzburgitic compositions that are locally intruded by pyroxenite dykes and dunite patches (Fig. 3). The dykes are normally less than 2 m thick and the patches are 2-3 m in size. In addition, the rare occurrence of transitional to alkaline dykes, dated at 40-38 Ma, has been documented by Delaloye and Desmons (1980).

The intrusive sequence is represented by two different gabbroic units: gabbros largely characterized by pegmatoid texture (hereafter named Pegmatoid Gabbro Unit) and gabbros showing foliated texture (hereafter named Foliated Gabbro Unit), which crop out in the NW and SE parts of the study area, respectively (Fig. 2). The pegmatoid gabbros are associated with abundant troctolites layers, whereas the foliated gabbros are associated with wehrlites and scarce troctolites (Fig. 3). In both gabbro types, troctolites occur as small (<2 m) layers and locally show distinct banding due to parallel layers with different modal proportions of olivine and plagioclase. Wehrlites form small layers (<1 m) at the base of the Foliated Gabbro Unit and locally show mylonitic texture. The Geological map of Harsin (Shahidi and Nazari, 1997) also reports the occurrence of ophiolitic layered gabbros and associated peridotites ~20 km SE of Sahneh (Fig. 2). Nonetheless, the field observations made by one of the authors of this paper (K. Allahyari) allowed to recognize that these rocks, differently from the other ophiolitic gabbros

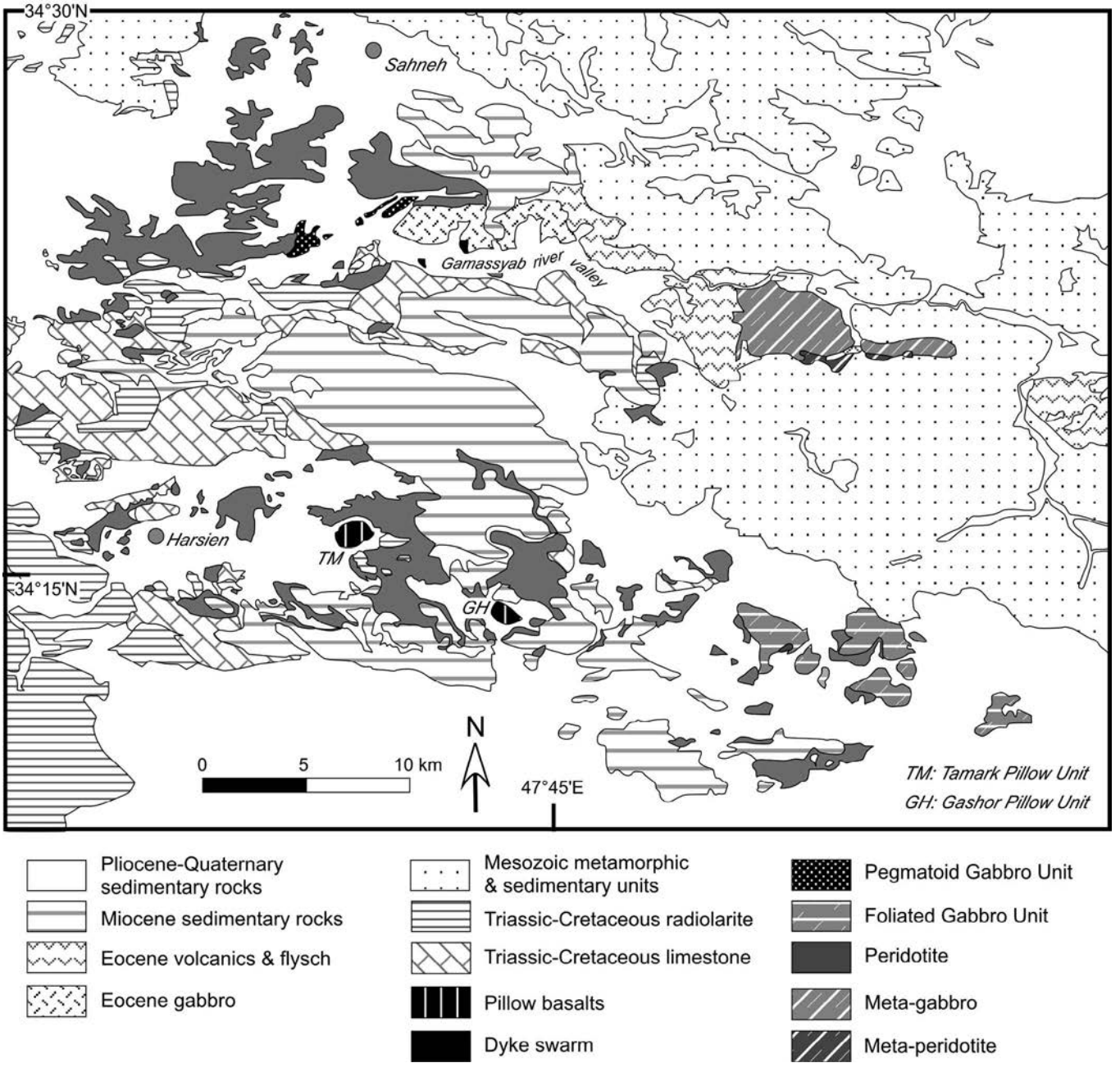

Fig. 2 - Simplified geological map of the Kermanshah ophiolitic complex (modified after Shahidi and Nazari, 1997).

and peridotites of the Kermanshah area, underwent dynamic metamorphic conditions. Field observations also indicate that these rocks cannot be related to the ophiolitic gabbros cropping out in the Kermanshah area and therefore they will not be considered in this paper.

The dyke complex surfaces in two very small outcrops in the Gamassyab River valley (Fig. 2). Because of the small dimensions of the outcrops, the intense tectonization and the widespread Quaternary sedimentary cover, it is not possible to establish if these dykes represent a portion of a typical ophiolitic sheeted dyke complex.

The volcanic rocks are scarce, as they only surface in two small outcrops in the southern part of the study area. They mainly consist of pillow basalts with very subordinate massive lava flows and basaltic breccias (Fig. 3). In both outcrops, the pillows are very different in size (from few decimetres to 1 metre in diameter) and are locally vesicular. Thin layers (5-10 cm) of radiolarites are locally intercalated in the pillows. According to Ghazi and Hassanipak (1999), these volcanic rocks are represented by alkaline basalts and trachytes, as well as by sub-alkaline basalts with island arc affinity. These authors suggested that the Kermanshah volcanic rocks represent off-axis volcanic units generated in within-plate, oceanic and island arc settings. The small amount of radiometric data available for some diabases yielded ages ranging from 83 to 86 Ma (Delaloye and Desmons, 1980).

Because of the mélange nature of the ophiolitic blocks and of the widespread Pliocene-Quaternary sedimentary cover, in many places of the Kermanshah area the relationships between the various ophiolitic rock-types cannot be established. Generally, each ophiolitic type is represented

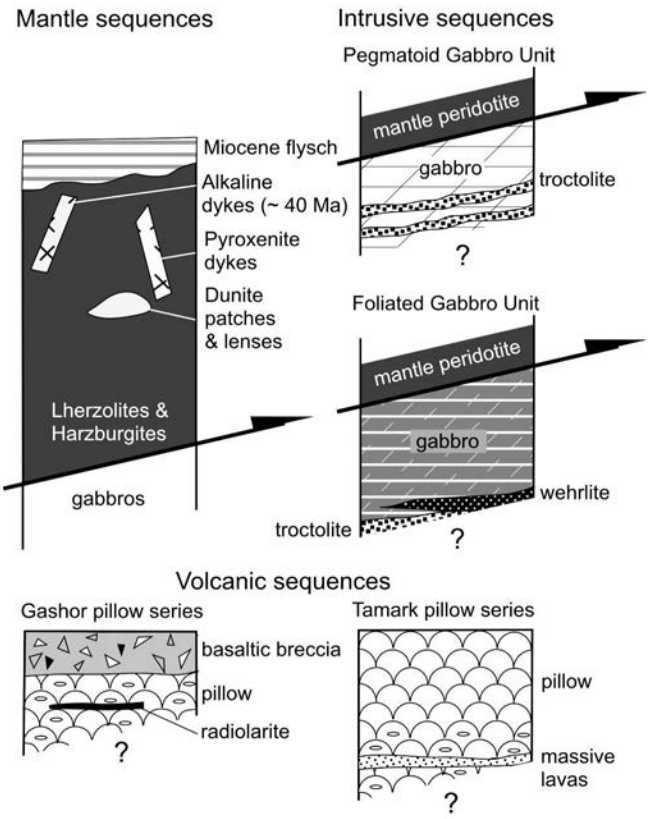

Fig. 3 - Simplified columnar sections of the main rock-types cropping out in the Kermanshah ophiolitic complex.

by individual blocks in the Pliocene-Quaternary sedimentary cover. No systematic distribution of lherzolites and harzburgites has been noticed in the field. Only in a few localities, tectonic contacts between gabbros (at the bottom) and mantle peridotites (at the top) can be observed (Figs. 3, 4). No sedimentary cover stratigraphically overlaying the various ophiolitic rocks can be observed in the Kermanshah area. In particular, though some radiolarite layers are interbedded within pillow basalts, there is no direct evidence that suggest that Maastrichtian radiolarites represent the original sedimentary cover of the ophiolite sequence. Moreover, in some places (Fig. 2), mantle tectonites are overlain by unconformable Miocene sedimentary rocks (Figs. 3, 4).

PETROGRAPHY

The main petrographic characteristics of the rocks studied in this paper are summarized in Table 1. Mantle tectonites consist of lherzolites (very subordinate) and harzburgites (largely prevailing). Based on modal composition, two types of harzburgites can, in turn, be recognized: cpx-free harzburgites and cpx-rich harzburgites (with clinopyroxene modal content = 3-5%). Texturally, all tectonite varieties display many similarities, with the only exception being the porphyroclastic texture, which is only observed in harzburgites. Olivine commonly appears as either porphyroclasts (up to 8 mm in size) in harzburgites or as large grains (~3-5 mm) in both harzburgites and lherzolites and exhibits kink banding. Nonetheless, fine-grained olivine (<1 mm) is also observed in lherzolites. Orthopyroxene is commonly 1-2 mm, but may also form porphyroclasts up to 6 mm in size in harzburgites. Clinopyroxene appears either as isolated grains in cpx-rich harzburgites or as aggregates in lherzolites and is variable in size (<1-3 mm). In all rock-types, both orthopyroxene and clinopyroxene show exsolution lamellae, kink banding and curved cleavage. Moreover, clinopyroxene is often characterized by corroded boundaries. Cr-spinel is a ubiquitous accessory mineral in all peridotites, where it occurs as lobate or subhedral small (<1 mm) crystals. The primary minerals of the mantle tectonites have been altered to varying degrees into secondary assem-

Table 1 - Summary of the main petrographic characteristics of the ophiolitic rocks from the Kermanshah ophiolitic complex.

Rock type	Rock Texture	Modal Composition (%)	Alteration Degree	Alteration Minerals
Lherzolite	equigranular / inequigranular; mesh	ol 45–50; opx 10–15; cpx 25–30; Cr-sp <5	high (moderate)	serp; chl Fe-ox
Harzburgite	equigranular; porphyroclastic; mesh	ol 50–55; opx 40-45; cpx <5; Cr-sp <5	high (moderate)	serp; Fe-ox
Dunite	orthocumulitic / adcumulitic; mesh	ol 90–95; cpx <2; pl <5; Cr-Sp <1	very high	serp; chl; sau Fe-ox
Wehrlite	orthocumulitic	ol 35–40; opx <5 cpx 55–65	high	serp; chl Fe-ox
Troctolite	cumulitic	ol 60–40; pl 60–40 Cpx <5	high	serp; cc; clay min
Pegmatoid gabbro & olivine-gabbro	cumulitic / (granular) poikilitic coarse-grained	pl 50–60; cpx 30–40; opx 0–3; ol 0–25; ox 0-8	high (moderate)	serp; cc; act; clay min
Foliated gabbro & olivine-gabbro	granular / with foliataion	pl 50–60; cpx 30–40; opx 0–3; ol 0–15; ox 0-8	high (moderate)	serp; clay min; Ti-par; act; prh

Abbreviations, ol: olivine; cpx: clinopyroxene; opx: orthopyroxene; Cr-sp: Cr-spinel; pl: plagioclase; ox: oxides; serp: serpentine; chl: chlorite; Fe-ox: Fe-oxides; sau: saussurite; cc: calcite; clay min: clay minerals; Ti-par: Ti-pargasite; act: actinolite; (): rare occurrence.

blages (Table 1). Several samples display mesh texture, where relicts of olivine and pyroxene are included in a serpentinites matrix.

Dunites display cumulitic texture, in which olivine is the cumulus phase and plagioclase and/or clinopyroxene are the intercumulus phases. Wehrlites and troctolites are also cumulitic in texture. In wehrlites, the cumulus and intercumulus phases are represented by olivine and by clinopyroxene and rare orthopyroxene, respectively. Troctolites are characterized by euhedral olivine, subhedral plagioclase, and small amounts of anhedral clinopyroxene.

Pegmatoid gabbros, which are generally coarse grained in nature, show cumulitic texture. Nonetheless, a few samples from the pegmatoid gabbro unit show medium-grained, isotropic texture. In the cumulate varieties, the poikilitic texture is observed locally. The mineral assemblage of the cumulate gabbros is characterized by various proportions of olivine, plagioclase, clinopyroxene, and Fe-Ti-oxides as accessory phases. Isotropic gabbros have granular texture and a mineral assemblage including plagioclase, clinopyroxene, and relatively abundant Fe-Ti-oxides.

The texture of the medium to fine grained foliated gabbros is characterized by magmatic foliation marked by the preferred orientation of the rock-forming minerals. The mineral assemblage is represented by elongated crystals of plagioclase, clinopyroxene, and sometimes olivine. Fe-Ti-oxides are ubiquitous accessory phases. In some samples, clinopyroxene oikocrysts enclose olivine and elongated crystals of plagioclase.

In all gabbroic varieties, the crystallization order is: olivine → plagioclase → clinopyroxene ± Fe-Ti-oxides, which is the typical crystallization order of mid-ocean ridge type (MORB) ophiolites (Beccaluva et al., 1983).

ANALYTICAL METHODS

Major element compositions of minerals were determined by electron probe micro-analysis (EPMA) using a Cameca CAMEBAX instrument, at the Istituto di Geoscienze e Georisorse, CNR, Padua (Italy). The acceleration voltage and sample current were 15 keV and 20 μA, respectively, and the counting time was 100 s. Instrumental calibration was made using natural and synthetic minerals as standards. Matrix corrections were performed using the PAP method (Pouchou and Pichoir, 1985). Analytical precision was better than ±2% for elements in the range 10-20wt% oxide, better than 5% for elements in the range 2-10wt% oxide, and better than 10% for elements in the range 0.5-2wt% oxide. Representative analyses are reported in Tables 2-5.

Whole-rock major and some trace elements (Zn, Cu, Sc, Ga, Ni, Co, Cr, V, Rb, Ba, Nb, La, Sr, Zr, Y) were obtained by X-ray fluorescence (XRF) on pressed-powder pellets, using an ARL Advant-XP automated X-ray spectrometer. Calibration was made using international reference samples and the matrix correction method proposed by Lachance and Trail (1966) was applied. Accuracy and detection limits were determined using international reference standards run as unknowns. Mean accuracies were generally better than 2% for major oxides, and 5% for trace element determinations, while the detection limits for trace elements were: Zn, Ba, Cu, Sc = 5 ppm; Ga, Ni, Co, Cr, V, Sr, Nb, La, Zr = 2 ppm; Rb, Y = 1 ppm. Volatile contents were determined as loss on ignition at 1000°C.

In addition, Rb, Sr, Y, Zr, Nb, Hf, Ta, Th, and U, and the rare earth elements (REE) were determined by inductively coupled plasma-mass spectrometry (ICP-MS) using a Thermo Series X-I spectrometer. The accuracy of the data and detection limits were evaluated using results for international standard rocks and the blind standards included in the sample set. Accuracy ranged from 2 to 7 relative percent, with the exception of Nb and Ta (12%), and U (9%). Detection limits (in ppm) were: Rb, Sr, Y, Zr, Nb = 0.02; Hf, Ta, Th, U = 0.002; La, Ce = 0.005; Pr, Nd, Sm, Eu, Gd, Tb, Dy, Ho, Er, Tm, Yb, Lu = 0.002. All whole-rock analyses were performed at the Dipartimento di Science della Terra, Università di Ferrara. Representative analyses are reported in Tables 6 and 7.

MINERAL CHEMISTRY

Spinel

Cr-spinel is restricted to the mantle tectonites and associated ultramafic cumulates. Representative analyses of spinel from the mantle peridotites are presented in Table 2. Cr-spinels in lherzolites show quite uniform compositions, particularly for TiO_2, Al_2O_3 and Cr_2O_3 contents. They show relatively low Cr# [100xCr/(Cr+Al)] and Fe# [100xFe^{2+}/(Fe^{2+}+Mg)] (Fig. 5). In Fig. 5 it can be observed that they plot in the field for abyssal peridotites (Dick and Bullen, 1984). By contrast, Cr-spinels in cpx-rich harzburgites are characterized by rather variable compositions (Table 2). Also Cr# and Fe# are rather variable (Fig. 5). In particular, Cr-spinels from cpx-rich harzburgite K2 show the highest Cr# and Fe#. By contrast, Cr-spinels from cpx-rich harzburgite K202 display compositions that are characterized by relatively low Cr# and relatively high Mg# (Table 2). Cr-spinels in cpx-free harzburgites and dunites show more uniform compositions, when compared with those in cpx-rich harzburgites. All Cr-spinels from harzburgitic rocks and dunites show Cr# and Fe# similar to those of Cr-spinels from supra-subduction zone (SSZ) peridotites (Fig. 5).

Olivine

Representative olivine analyses from mantle peridotites and foliated gabbros are presented in Table 3. Olivine is generally unzoned. All olivines of the mantle peridotites exhibit a forsterite content of >90%. They show an evolution trend with increasing forsterite content from lherzolites (90.1-90.3%) to cpx-rich harzburgites (90.4-91.5%),

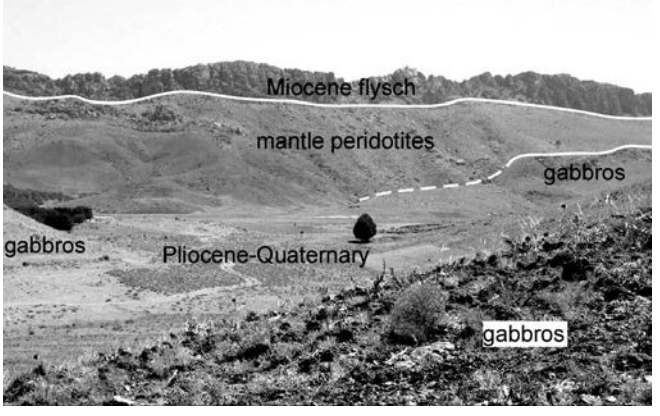

Fig. 4 - Outcrop view of the mantle peridotites, their Miocene flysch discordant cover, and the tectonically underlying Pegmatoid Gabbro Unit. The Photo was taken south of Sahneh towards NE.

Table 2 - Representative analyses of chromian spinels from the mantle peridotites of the Kermanshah ophiolitic complex.

Rock	lh	lh	lh	cpx-hz	cpx-hz	cpx-hz	cpx-hz	cpx-hz	cpx-hz	hz	hz	hz	hz	du
Sample	K1	K51	K51	K87	K19	K2	K202	K86	K205	K44	K44	K204	K101	K15
Mineral	sp 2	sp 1-1r	sp 2-3	sp 7	sp 1c	sp 4-1c	sp 8-2	sp 1	sp 8	sp 7-1	sp 2	sp 2	sp 4	sp 1-4
SiO_2	0.07	0.02	0.04	0.07	0.14	0.04	0.04	0.05	0.02	0.04	0.02	0.03	0.05	0.48
TiO_2	0.04	0.03	0.03	0.02	0.02	0.05	0.05	0.02	0.01	0.02	0.03	0.03	0.03	0.03
Al_2O_3	46.28	45.08	46.93	26.70	20.32	14.94	31.69	27.01	22.57	21.85	22.70	26.35	23.05	18.78
Cr_2O_3	23.72	24.93	22.87	43.59	47.66	53.96	39.08	43.06	48.11	47.39	45.62	44.07	44.96	53.03
FeO	14.26	12.85	12.79	16.44	16.87	21.81	15.21	15.20	17.18	18.57	18.45	16.96	19.63	15.55
MnO	0.00	0.12	0.17	0.00	0.00	0.36	0.18	0.26	0.28	0.30	0.25	0.23	0.28	0.29
MgO	16.92	18.07	17.95	13.80	13.37	9.70	15.49	14.84	12.39	12.42	12.69	13.87	12.04	11.28
CaO	0.00	0.00	0.00	0.00	0.01	0.03	0.00	0.00	0.00	0.03	0.00	0.00	0.06	0.00
NiO	0.21	0.26	0.24	0.09	0.06	0.06	0.16	0.14	0.07	0.06	0.04	0.08	0.09	0.05
Total	101.52	101.36	101.03	100.73	98.45	100.96	101.90	100.59	100.64	100.68	99.80	101.63	100.19	99.49
a.p.f.u.														
Si	0.002	0.000	0.001	0.002	0.004	0.001	0.001	0.002	0.001	0.001	0.001	0.001	0.001	0.015
Ti	0.001	0.001	0.001	0.000	0.000	0.001	0.001	0.001	0.000	0.000	0.001	0.001	0.001	0.001
Al	1.478	1.437	1.492	0.940	0.749	0.565	1.073	0.944	0.816	0.791	0.823	0.922	0.836	0.696
Cr	0.508	0.533	0.488	1.029	1.179	1.370	0.888	1.010	1.167	1.151	1.110	1.034	1.093	1.318
Fe^{3+}	0.008	0.027	0.017	0.025	0.062	0.060	0.034	0.041	0.016	0.055	0.064	0.041	0.067	0.000
Fe^{2+}	0.315	0.264	0.271	0.386	0.379	0.526	0.331	0.336	0.425	0.423	0.411	0.380	0.439	0.409
Mn	0.000	0.003	0.004	0.000	0.000	0.010	0.004	0.007	0.007	0.008	0.006	0.006	0.007	0.008
Mg	0.683	0.729	0.722	0.615	0.623	0.464	0.663	0.656	0.567	0.569	0.582	0.614	0.552	0.529
Ca	0.000	0.000	0.000	0.000	0.000	0.001	0.000	0.000	0.000	0.001	0.000	0.000	0.002	0.000
Ni	0.005	0.006	0.005	0.002	0.001	0.002	0.004	0.003	0.002	0.001	0.001	0.002	0.002	0.001
Total	3.000	3.000	3.000	3.000	3.000	3.000	3.000	3.000	3.000	3.000	3.000	3.000	3.000	2.977
Mg#	0.68	0.73	0.73	0.61	0.62	0.47	0.67	0.66	0.57	0.57	0.59	0.62	0.56	0.56
Cr#	0.26	0.27	0.25	0.52	0.61	0.71	0.45	0.52	0.59	0.59	0.57	0.53	0.57	0.65

Abbreviations, lh: lherzolite; cpx-hz: clinopyroxene-rich harzburgite; hz: clinopyroxene-free harzburgite; du: dunite. Mg# = $Mg/(Mg+Fe^{2+})$; Cr# = Cr/(Cr+Al). The compositions of Fe^{3+} and Fe^{2+} were calculated from the measured total FeO according to Droop (1987).

Table 3 - Representative analyses of olivines from mantle peridotites and mafic intrusive rocks of the Kermanshah ophiolitic complex.

Rock	lh	lh	cpx-hz	cpx-hz	cpx-hz	cpx-hz	cpx-hz	cpx-hz	hz	hz	du	ol-gb	ol-gb
Sample	K01	K01	K87	K19	K02	K202	K86	K205	K44	K204	K15	K62	K315
Mineral	ol 2	ol 3	ol 2	ol 2	ol 2-2	ol 8-2	ol 10	ol 2	ol 7-1	ol 3	ol 2-1	ol 5	ol 2
SiO_2	41.34	41.19	41.40	41.26	41.32	41.36	41.07	40.84	41.17	41.02	41.49	39.19	40.11
TiO_2	0.00	0.01	0.00	0.01	0.00	0.00	0.00	0.00	0.00	0.01	0.00	0.01	0.00
Al_2O_3	0.00	0.00	0.00	0.00	0.01	0.00	0.02	0.00	0.00	0.00	0.00	0.00	0.00
Cr_2O_3	0.00	0.04	0.00	0.02	0.03	0.00	0.02	0.00	0.04	0.00	0.00	0.02	0.02
FeO	9.40	9.57	8.91	9.20	8.59	8.77	8.80	8.93	7.84	8.90	6.88	22.61	16.84
MnO	0.13	0.16	0.18	0.16	0.15	0.12	0.11	0.16	0.12	0.13	0.09	0.29	0.26
MgO	49.68	49.76	49.74	49.82	50.34	50.29	50.01	49.79	51.59	50.43	51.93	39.99	44.10
CaO	0.00	0.03	0.05	0.02	0.02	0.00	0.05	0.02	0.00	0.00	0.04	0.04	0.04
Na_2O	0.00	0.03	0.00	0.00	0.01	0.02	0.00	0.03	0.02	0.00	0.00	0.00	0.00
NiO	0.39	0.38	0.40	0.40	0.47	0.44	0.38	0.40	0.41	0.40	0.43	0.11	0.18
Total	100.95	101.16	100.69	100.90	100.93	101.02	100.46	100.17	101.19	100.88	100.86	102.27	101.57
a.p.f.u.													
Si	1.002	0.998	1.004	1.000	0.999	1.000	0.998	0.997	0.990	0.994	0.996	0.996	1.000
Ti	0.000	0.000	0.000	0.000	0.000	0.000	0.000	0.000	0.000	0.000	0.000	0.000	0.000
Al	0.000	0.000	0.000	0.000	0.000	0.000	0.001	0.000	0.000	0.000	0.000	0.000	0.000
Cr	0.000	0.001	0.000	0.000	0.001	0.000	0.000	0.000	0.001	0.000	0.000	0.000	0.000
Fe^{2+}	0.191	0.194	0.181	0.186	0.174	0.177	0.179	0.182	0.158	0.180	0.138	0.481	0.351
Mn	0.003	0.003	0.004	0.003	0.003	0.002	0.002	0.003	0.002	0.003	0.002	0.006	0.006
Mg	1.795	1.797	1.798	1.800	1.815	1.812	1.812	1.812	1.850	1.821	1.859	1.516	1.639
Ca	0.000	0.001	0.001	0.000	0.000	0.000	0.001	0.000	0.000	0.000	0.001	0.001	0.001
Na	0.000	0.001	0.000	0.000	0.000	0.001	0.000	0.002	0.001	0.000	0.000	0.000	0.000
Ni	0.008	0.007	0.008	0.008	0.009	0.009	0.007	0.008	0.008	0.008	0.008	0.002	0.004
Total	2.998	3.002	2.996	2.999	3.001	3.001	3.001	3.004	3.010	3.006	3.004	3.003	3.000
Fo %	90.3	90.1	90.7	90.5	91.1	91.0	90.9	90.7	92.0	90.9	93.0	75.7	82.1
Fa %	9.6	9.7	9.1	9.4	8.7	8.9	9.0	9.1	7.8	9.0	6.9	24.0	17.6
Mg#	0.90	0.90	0.91	0.91	0.91	0.91	0.91	0.91	0.92	0.91	0.93	0.76	0.82

Abbreviations, lh: lherzolite; cpx-hz: clinopyroxene-rich harzburgite; hz: clinopyroxene-free harzburgite; du: dunite; ol-gb: olivine-gabbro; ol: olivine; Fo: forsterite; Fa: fayalite. Mg# = $Mg/(Mg+Fe^{2+})$.

Table 4 - Representative analyses of pyroxenes from mantle peridotites and mafic intrusive rocks of the Kermanshah ophiolitic complex.

	orthopyroxene												
Rock	lh	lh	cpx-hz	cpx-hz	cpx-hz	cpx-hz	cpx-hz	cpx-hz	cpx-hz	cpx-hz	hz	hz	hz
Sample	K01	K01	K87	K19	K02	K86	K205	K205	K202	K202	K44	K44	K204
Mineral	opx 2	opx 3	opx 1	opx 7	opx 5-1	opx 13	opx 3	opx 8	opx 1-2	opx 4-2	opx 6-3	opx 2-1	opx 1
SiO_2	55.70	55.57	56.81	56.72	56.98	56.01	56.16	55.99	56.27	56.07	57.08	56.22	55.76
TiO_2	0.03	0.01	0.02	0.00	0.00	0.00	0.01	0.04	0.00	0.05	0.00	0.01	0.00
Al_2O_3	3.56	3.89	2.15	1.75	0.98	2.39	1.80	1.91	2.47	2.53	1.33	1.94	2.07
Cr_2O_3	0.59	0.77	0.70	0.69	0.39	0.83	0.56	0.76	0.63	0.82	0.25	0.81	0.65
FeO	6.39	6.04	5.95	5.84	5.95	5.79	6.05	5.71	5.78	5.59	5.83	5.41	5.59
MnO	0.11	0.12	0.20	0.15	0.15	0.15	0.14	0.15	0.15	0.13	0.17	0.14	0.11
MgO	33.19	33.26	33.42	33.41	35.25	33.94	34.97	34.54	34.42	33.63	35.59	34.29	34.46
CaO	0.63	0.68	1.37	1.72	0.77	1.32	0.75	0.59	1.10	2.38	0.51	1.89	0.95
Na_2O	0.03	0.02	0.00	0.01	0.00	0.01	0.00	0.00	0.00	0.00	0.00	0.02	0.00
K_2O	0.00	0.00	0.00	0.00	0.00	0.01	0.00	0.01	0.00	0.00	0.00	0.00	0.00
Total	100.23	100.36	100.62	100.28	100.47	100.46	100.44	99.70	100.81	101.18	100.75	100.74	99.59
a.p.f.u.													
Si	1.920	1.912	1.951	1.956	1.950	1.923	1.923	1.932	1.922	1.914	1.944	1.922	1.925
Ti	0.001	0.000	0.001	0.000	0.000	0.000	0.000	0.001	0.000	0.001	0.000	0.000	0.000
Al	0.145	0.158	0.087	0.071	0.039	0.097	0.072	0.078	0.099	0.102	0.053	0.078	0.084
Cr	0.016	0.021	0.019	0.019	0.011	0.023	0.015	0.021	0.017	0.022	0.007	0.022	0.018
Fe^{3+}	0.000	0.000	0.000	0.000	0.051	0.035	0.067	0.035	0.040	0.046	0.053	0.057	0.049
Fe^{2+}	0.184	0.174	0.171	0.168	0.119	0.131	0.107	0.130	0.125	0.113	0.113	0.098	0.113
Mn	0.003	0.004	0.006	0.004	0.004	0.004	0.004	0.004	0.004	0.004	0.005	0.004	0.003
Mg	1.706	1.706	1.711	1.718	1.798	1.737	1.785	1.777	1.752	1.711	1.807	1.748	1.774
Ca	0.023	0.025	0.050	0.063	0.028	0.049	0.027	0.022	0.040	0.087	0.019	0.069	0.035
Na	0.002	0.001	0.000	0.001	0.000	0.001	0.000	0.000	0.000	0.000	0.000	0.002	0.000
K	0.000	0.000	0.000	0.000	0.000	0.000	0.000	0.000	0.000	0.000	0.000	0.000	0.000
Total	4.000	4.000	3.995	4.000	4.000	4.000	4.000	4.000	4.000	4.000	4.000	4.000	4.000
Wo %	1.2	1.3	2.6	3.3	1.4	2.5	1.4	1.1	2.1	4.4	0.9	3.5	1.8
En %	89.1	89.5	88.5	88.1	90.1	89.0	89.9	90.5	89.5	87.4	90.7	88.6	90.0
Fs %	9.6	9.1	8.8	8.6	8.5	8.5	8.7	8.4	8.4	8.1	8.3	7.8	8.2
Acm %	0.1	0.1	0.0	0.0	0.0	0.0	0.0	0.0	0.0	0.0	0.0	0.1	0.0
Mg#	0.90	0.91	0.91	0.91	0.91	0.91	0.91	0.92	0.91	0.92	0.92	0.92	0.92

	clinopyroxene										
Rock	lh	lh	cpx-hz	cpx-hz	cpx-hz	ol-gb	ol-gb	ol-gb	ol-gb	gb	gb
Sample	K51	K51	K87	K86	K205	k62A	k62A	K315	K315	K36	K36
Mineral	cpx 1-1	cpx 2-2	cpx 1	cpx 2	cpx 2	cpx 1	cpx 6	cpx 3r	cpx 9c	cpx 1c	cpx 1r
SiO_2	51.68	52.16	53.34	52.64	53.01	52.36	51.93	52.93	53.09	52.62	52.91
TiO_2	0.11	0.09	0.04	0.03	0.00	0.69	0.73	0.37	0.35	0.40	0.29
Al_2O_3	4.10	3.58	2.43	2.38	1.58	2.83	3.05	2.14	2.89	1.64	2.39
Cr_2O_3	1.01	0.79	0.93	1.13	0.61	0.16	0.12	0.34	0.23	0.08	0.13
FeO	2.44	2.53	2.24	2.16	1.80	5.93	5.71	4.26	4.71	7.07	7.72
MnO	0.10	0.10	0.07	0.08	0.10	0.17	0.12	0.08	0.07	0.26	0.22
MgO	17.18	18.46	17.22	17.69	17.90	15.91	15.67	16.49	15.86	15.09	15.00
CaO	22.79	22.36	23.52	23.61	24.10	21.67	22.20	22.62	22.51	22.34	20.82
Na_2O	0.21	0.13	0.04	0.00	0.00	0.33	0.54	0.46	0.53	0.11	0.28
K_2O	0.00	0.00	0.00	0.00	0.02	0.00	0.00	0.01	0.00	0.00	0.01
Total	99.62	100.19	99.82	99.72	99.13	100.06	100.05	99.68	100.25	99.59	99.77
a.p.f.u.											
Si	1.880	1.880	1.940	1.916	1.937	1.921	1.902	1.936	1.935	1.955	1.957
Ti	0.003	0.002	0.001	0.001	0.000	0.019	0.020	0.010	0.010	0.011	0.008
Al	0.176	0.152	0.104	0.102	0.068	0.122	0.132	0.092	0.124	0.072	0.104
Cr	0.029	0.022	0.027	0.032	0.018	0.005	0.004	0.010	0.007	0.002	0.004
Fe^{3+}	0.044	0.071	0.000	0.032	0.041	0.016	0.060	0.037	0.018	0.002	0.000
Fe^{2+}	0.031	0.005	0.068	0.034	0.014	0.166	0.115	0.093	0.126	0.218	0.239
Mn	0.003	0.003	0.002	0.003	0.003	0.005	0.004	0.002	0.002	0.008	0.007
Mg	0.932	0.992	0.934	0.960	0.975	0.870	0.856	0.899	0.862	0.836	0.827
Ca	0.888	0.863	0.916	0.921	0.944	0.852	0.871	0.887	0.879	0.889	0.825
Na	0.015	0.009	0.003	0.000	0.000	0.024	0.038	0.032	0.038	0.008	0.020
K	0.000	0.000	0.000	0.000	0.001	0.000	0.000	0.000	0.000	0.000	0.000
Total	4.000	4.000	3.995	4.000	4.000	4.000	4.000	4.000	4.000	4.000	3.991
Wo %	46.5	44.5	47.7	47.3	47.8	44.2	44.9	45.5	45.7	45.5	43.2
En %	48.8	51.1	48.6	49.3	49.4	45.1	44.1	46.1	44.8	42.8	43.3
Fs %	3.9	3.9	3.5	3.4	2.8	9.4	9.0	6.7	7.5	11.2	12.5
Acm %	0.8	0.5	0.1	0.0	0.0	1.2	2.0	1.7	2.0	0.4	1.0
Mg#	0.93	0.93	0.93	0.94	0.95	0.83	0.83	0.87	0.86	0.79	0.78

Abbreviations, lh: lherzolite; cpx-hz: clinopyroxene-rich harzburgite; hz: clinopyroxene-free harzburgite; ol-gb: olivine-gabbro; gb: gabbro; cpx: clinopyroxene; opx: orthopyroxene; c: core; r: rim; Wo: wollastonite; En: enstatite; Fs: ferrosilite; Acm: acmite. Mg# = $Mg/(Mg+Fe^{2+})$. The compositions of Fe^{3+} and Fe^{2+} were calculated from the measured total FeO according to Droop (1987).

Table 5 - Representative analyses of plagioclases from mafic intrusive rocks of the Kermanshah ophiolitic complex.

Rock	ol-gb	ol-gb	ol-gb	ol-gb	gb	gb
Sample	K62A	K62A	K315	K315	K36	K36
Mineral	pl 1c	pl 1r	pl 5	pl 7	pl 6	pl 10
SiO_2	51.97	51.49	49.14	47.59	48.61	49.59
TiO_2	0.03	0.01	0.02	0.01	0.05	0.06
Al_2O_3	30.84	31.23	33.25	33.77	32.52	31.78
Cr_2O_3	0.00	0.00	0.02	0.06	0.00	0.01
FeO	0.23	0.17	0.17	0.21	0.39	0.42
MnO	0.01	0.01	0.00	0.00	0.01	0.04
MgO	0.00	0.00	0.00	0.00	0.02	0.07
CaO	13.27	13.69	15.73	16.35	15.75	14.24
Na_2O	3.91	3.70	2.57	2.04	2.65	3.32
K_2O	0.09	0.12	0.05	0.05	0.02	0.00
Total	100.35	100.43	100.95	100.08	100.02	99.54
a.p.f.u.						
Si	2.352	2.331	2.225	2.179	2.227	2.274
Ti	0.001	0.000	0.001	0.000	0.002	0.002
Al	1.645	1.667	1.775	1.823	1.756	1.718
Cr	0.000	0.000	0.001	0.002	0.000	0.000
Fe^{2+}	0.009	0.006	0.006	0.008	0.015	0.016
Fe^{3+}	0.000	0.000	0.000	0.000	0.000	0.000
Mn	0.000	0.000	0.000	0.000	0.000	0.002
Mg	0.000	0.000	0.000	0.000	0.001	0.005
Ca	0.643	0.664	0.763	0.802	0.773	0.700
Na	0.343	0.325	0.226	0.181	0.236	0.296
K	0.005	0.007	0.003	0.003	0.001	0.000
Total	4.999	5.001	5.000	4.999	5.011	5.012
Ab %	34.6	32.6	22.8	18.4	23.3	29.7
An %	64.9	66.7	76.9	81.3	76.6	70.3
Or %	0.5	0.7	0.3	0.3	0.1	0.0

Abbreviations, ol-gb: olivine-gabbro; gb: gabbro; pl: plagioclase; c: core; r: rim; Ab: albite; An: anorthite; Or: orthoclase.

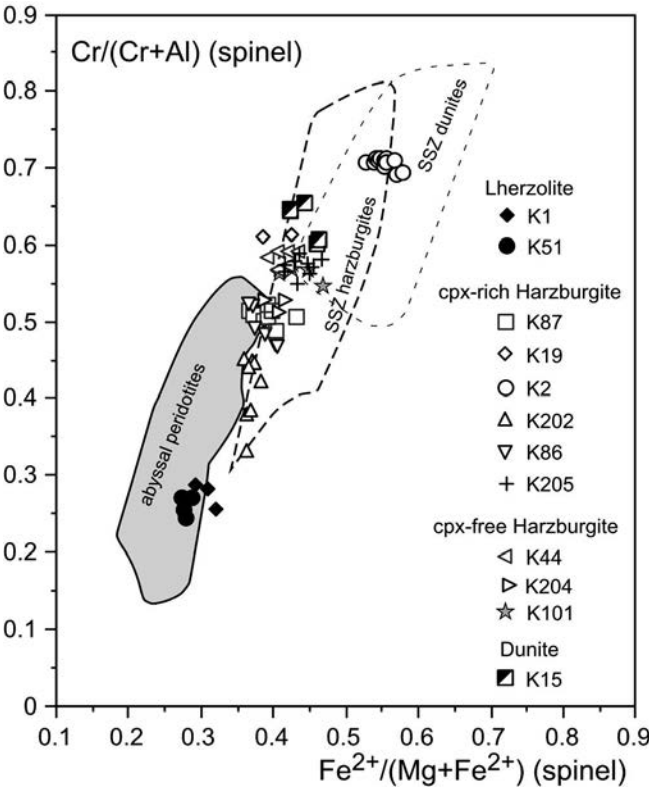

Fig. 5 - Cr# vs. Fe# diagram for spinels from mantle peridotites of the Kermanshah ophiolitic complex. Compositional variations for abyssal spinel peridotite (Dick and Bullen, 1984) and supra-subduction zone (SSZ) harzburgites and dunites (Ishii et al., 1992) are also reported.

cpx-free harzburgites (90.9-92.0%) and dunites (92.8-93.0%). Olivine from the different mantle peridotites and associated dunites shows similar NiO contents, though they are rather variable within each rock type (0.36-0.39wt% in lherzolites; 0.35-0.47wt% in cpx-rich harzburgites; 0.33-0.45wt% in cpx-free harzburgites; 0.37-0.47wt% in dunites). Olivine in gabbros displays variable forsterite contents, though they have quite uniform composition within each sample (Table 3). NiO content is somewhat related to the forsterite contents, ranging from 0.10 to 0.17wt% and from 0.16 to 0.23wt% in gabbros K62A and K315, respectively. The variability of NiO in the various rock types can be related to the segregation of olivine from melts at different stages of fractionation. Olivine with high NiO content crystallized from relatively primitive magmas and vice versa. Moreover, a negative correlation between NiO and forsterite can be observed in the olivine from sample K315 (not shown), possibly reflecting the cumulitic nature of this mineral. The overall chemical composition of olivine in gabbros is similar to that of equivalent rocks from oceanic gabbros and from Albanian ophiolite gabbros (Koller et al., 2006).

Orthopyroxene

Representative analyses of orthopyroxene from mantle peridotites are presented in Table 4. The orthopyroxene is generally unzoned and, according to the classification of Morimoto (1989), is enstatite. No difference in terms of quadrilateral components can be observed among orthopyroxenes from mantle lherzolites, cpx-rich harzburgites, and cpx-free harzburgites. Most of the analysed elements display comparable concentrations in these distinct mantle rock-types, with the exception of Al_2O_3, which is comparatively higher in lherzolites (3.56-4.55wt%) than in cpx-rich harzburgites (0.34-3.25wt%) and cpx-free harzburgites (1.33-2.07wt%). CaO is significantly lower in lherzolites (0.39-0.92wt%) with respect to cpx-rich harzburgites (0.23-3.10wt%) and cpx-free harzburgites (0.51-2.86wt%). Mg# is slightly lower in lherzolites (90.3-90.8) than in cpx-rich harzburgites (90.8-91.7) and cpx-free harzburgites (91.2-91.9). Cr_2O_3 content is negligible in all peridotite types (<1wt.%).

The orthopyroxene from gabbro K315 has a higher ferrosilite component with respect to those of mantle peridotites. Accordingly, FeO is higher and Al_2O_3, CaO, Cr_2O_3, and Mg# are lower when compared to orthopyroxenes of mantle peridotites (Table 4).

Clinopyroxene

Representative analyses of clinopyroxene in mantle peridotites and gabbros are presented in Table 4. All clinopyroxenes in mantle peridotites are unzoned and are classified as diopside. In terms of quadrilateral components (Morimoto, 1989), no difference can be seen between orthopyroxenes from lherzolites and cpx-rich harzburgites. Clinopyroxene in mantle lherzolites is characterized by higher contents of TiO_2, Al_2O_3, and Na_2O and lower Mg# with respect to cpx-rich harzburgites (Table 4). With decreasing Mg#, TiO_2 content in clinopyroxenes from mantle peridotites increases gradually, while Na_2O and Al_2O_3 contents show a sharp increase. By contrast, CaO content sharply decreases with decreasing Mg#.

Table 6 - Representative major and trace element analyses of mantle peridotites from the Kermanshah ophiolitic complex.

Locality	Sahneh	Harsien	Harsien	Sahneh	Sahneh	Sahneh	Sahneh	Sahneh	Sahneh	Sahneh	Sahneh	Sahneh	Sahneh	Sahneh
Sample	K1	K46	K51	K2	K19	K86	K87	K202	K205	K17	K44	K204	K15	K201
Rock	lh	lh	lh	cpx-hz	cpx-hz	cpx-hz	cpx-hz	cpx-hz	cpx-hz	hz	hz	hz	du	du
XRF analyses:														
SiO_2	42.92	39.09	39.25	44.19	42.68	40.40	43.36	42.69	41.03	43.00	41.17	39.47	35.05	39.72
TiO_2	0.01	0.04	0.01	0.01	n.d.	n.d.	n.d.		n.d.	n.d.	0.01	n.d.	n.d.	n.d.
Al_2O_3	1.04	1.39	1.01	0.17	0.36	0.35	0.68	0.46	0.36	0.38	0.26	0.31	0.01	0.05
FeO	9.01	8.98	7.78	8.49	8.56	8.48	8.31	8.57	8.67	8.12	8.40	7.92	7.13	8.91
MnO	0.14	0.17	0.12	0.13	0.13	0.13	0.13	0.12	0.13	0.13	0.13	0.12	0.10	0.12
MgO	44.84	36.82	38.31	44.42	44.65	43.18	42.83	44.32	43.16	40.26	43.84	41.66	43.83	49.87
CaO	1.89	0.19	1.30	0.86	0.81	0.76	1.16	0.74	0.80	1.16	0.74	0.72	0.02	0.31
Na_2O	0.05	n.d.	n.d.	0.04	0.04	0.01	0.03	0.01	0.02	0.02	0.02	n.d.	n.d.	0.01
L.O.I.	0.00	13.28	12.15	1.53	2.73	6.61	3.39	3.06	5.76	6.97	5.38	9.78	13.91	0.97
Total	99.90	99.95	99.93	99.83	99.95	99.91	99.88	99.96	99.93	100.03	99.94	99.99	100.05	99.96
Mg#	89.9	88.0	89.8	90.3	90.3	90.1	90.2	90.2	89.9	89.8	90.3	90.4	91.6	90.9
Zn	43	49	34	33	39	31	32	32	27	34	39	28	19	14
Cu	18	30	19	n.d.	10	14	12	8	7	6	6	13	n.d.	n.d.
Sc	5	9	7	n.d.	n.d.	n.d.	5	n.d.	n.d.	6	5	n.d.	n.d.	n.d.
Ni	2366	2282	2055	2546	2494	2382	2257	2441	2387	2445	2347	2273	3127	2934
Co	103	101	85	116	111	99	102	105	97	106	103	92	93	119
Cr	3107	2436	2305	2153	2466	2299	2864	2120	2146	2169	2409	2391	546	2141
V	49	63	41	21	28	28	36	30	27	29	27	28	n.d.	6
Sr	3	5	7	12	n.d.	n.d.	n.d.	2	n.d.	4	n.d.	n.d.	2	13
Zr	n.d.	3	3	3	3	4	4	5	4	2	2	4	2	n.d.
Y	1	2	1	n.d.	n.d.	1	n.d.	1	1	n.d.	n.d.	n.d.	n.d.	n.d.
ICP-MS analyses:														
Rb	0.104	n.d.			0.144		0.694				0.225	0.198		0.086
Sr	2.15	4.49			0.342		1.83				0.295	0.348		10.3
Y	0.420	1.33			0.102		0.234				0.096	0.214		0.104
Zr	0.557	2.38			0.207		0.287				0.475	0.204		0.265
La	0.010	0.002			0.022		0.031				0.060	0.020		0.023
Ce	0.020	0.013			0.045		0.050				0.100	0.030		0.047
Pr	0.003	0.005			0.006		0.006				0.012	0.004		0.004
Nd	0.015	0.066			0.023		0.023				0.044	0.019		0.018
Sm	0.006	0.037			0.007		0.008				0.013	0.006		0.006
Eu	0.003	0.020			0.003		0.003				0.004	0.002		0.002
Gd	0.016	0.098			0.010		0.011				0.014	0.010		0.008
Tb	0.005	0.024			0.002		0.002				0.002	0.002		0.002
Dy	0.046	0.186			0.016		0.017				0.018	0.017		0.011
Ho	0.013	0.047			0.005		0.005				0.005	0.005		0.003
Er	0.046	0.160			0.017		0.018				0.019	0.017		0.012
Tm	0.008	0.026			0.003		0.004				0.003	0.003		0.003
Yb	0.062	0.190			0.023		0.032				0.029	0.024		0.018
Lu	0.012	0.028			0.004		0.006				0.006	0.004		0.003
Nb	0.029	0.180			0.034		0.064				0.050	0.078		0.051
Hf	0.007	0.022			0.003		0.004				0.008	0.005		0.007
Ta	0.003	0.019			0.009		0.007				0.009	0.012		0.007
Th	0.004	0.007			0.008		0.006				0.012	0.008		0.004
U	n.d.	0.004			0.003		0.002				0.005	n.d.		0.002
$(La/Sm)_N$	1.06	0.03			1.95		2.64				3.01	2.01		2.48
$(Sm/Yb)_N$	0.10	0.22			0.35		0.26				0.50	0.29		0.38
$(La/Yb)_N$	0.11	0.01			0.69		0.69				1.49	0.59		0.93

Abbreviations, lh: lherzolite; cpx-hz: clinopyroxene-rich harzburgite; hz: clinopyroxene-free harzburgite; du: dunite; n.d.: not detected. Mg# = 100xMg/(Mg+Fe). Normalizing values for REE ratios are from Sun and McDonough (1989).

Although clinopyroxene is the most widespread mineral in gabbros, it was analysed only in three samples because it is generally completely altered to amphibole (actinolite to Ti-pargasite). Clinopyroxenes plot across the diopside-augite field boundary (Morimoto, 1989). They show an evolution towards the ferrosilite end-member from olivine-gabbro to gabbro. Most clinopyroxenes in gabbros are unzoned. Nonetheless, a few crystals of gabbros from both Foliated and Pegmatoid Units exhibit an increase in TiO_2, Al_2O_3, and FeO contents from core to rim. Mg# values are generally high (83.6-87.4), while Cr_2O_3 content (0.04-0.40wt%) is relatively low and is negatively correlated with Mg#. By contrast, TiO_2 content is relatively high and varies from 0.35 to 0.73wt%.

TiO_2 content in mantle peridotites is generally low. However, the lowest contents are observed in cpx-rich harzburgites (<0.05wt%), when compared to lherzolites (0.09-0.11wt%). Pearce and Norry (1979) noted that Ti in clinopyroxenes reflects the degree of depletion of the mantle source, as well as the Ti activity of the parental magma that generated the intrusive rocks. The small Ti contents of the clinopyroxenes in the lherzolites suggest that a former partial melting event removed the Ti from the mantle clinopyroxenes, whereas the very low Ti contents of the clinopyroxenes in

Table 7 - Representative major and trace element analyses of mafic and ultramafic intrusive rocks from the Kermanshah ophiolitic complex.

Unit	Foliated Gabbro													Pegmatoid Gabbro							
Locality	H.Pa	H.Pa	H.Pa	H.Pa	H.Pa	H.Pa	H.Pa	H.Pa	H.Pa	H.Pa	H.Pa	H.Mj	S	S	S	S	S	S	S	S	
Sample	K59a	K302	K303	K305	K308	K309	K311	K313	K314	K315	K316	K62a	K20a	K105	K106	K20b	K36	K103	K102	K30	
Rock	wehrl.	ol-gb	ol-gb	ol-gb	ol-gb	ol-gb	ol-gb	gb	gb	ol-gb	gb	ol-gb	troct	troc	troc	ol-gb	gb	di	gb	Fe-gb	
Texture	cum	cum	cum	cum	cum	cum	cum	cum	cum	cum	isot	cum	cum	cum	cum	cum	cum	isot	cum	isot	
Note		top									bottom										
XRF analyses:																					
SiO_2	39.89	46.75	48.92	47.93	41.71	43.76	47.71	50.33	49.52	48.73	45.98	50.82	41.81	41.41	44.72	43.96	50.25	57.19	47.52	44.23	
TiO_2	0.09	0.17	0.26	0.22	0.06	0.11	0.18	0.29	0.22	0.19	1.98	0.33	0.02	0.04	0.05	0.02	0.19	0.39	0.15	1.16	
Al_2O_3	5.17	19.07	19.26	18.85	13.58	15.61	19.10	17.11	15.72	18.90	15.14	17.42	21.30	14.08	21.09	26.87	16.96	10.97	23.87	17.49	
Fe_2O_3		0.62	0.49	0.61	0.86	0.79	0.53	0.45	0.57	0.49	1.59	0.57	0.11	0.80	0.49	0.24	0.40	0.85	0.34	1.65	
FeO	9.30	4.12	3.27	4.04	5.76	5.24	3.50	2.97	3.79	3.26	10.62	3.81	0.75	5.31	3.30	1.59	2.64	5.69	2.24	10.98	
MnO	0.15	0.08	0.07	0.09	0.10	0.10	0.08	0.07	0.09	0.08	0.22	0.09	0.03	0.09	0.06	0.03	0.07	0.18	0.05	0.17	
MgO	32.16	12.46	8.38	10.77	22.82	19.82	10.69	9.03	12.10	9.77	7.29	8.57	6.19	21.42	11.86	7.43	9.01	11.15	5.75	7.27	
CaO	5.38	12.67	15.05	14.16	8.72	9.83	15.28	16.97	14.33	15.41	11.37	15.50	23.93	8.44	13.42	16.70	16.90	7.68	15.79	14.26	
Na_2O	0.10	1.62	2.18	1.81	0.45	0.87	1.60	1.88	1.76	1.88	2.33	2.42	0.11	0.42	0.95	1.26	1.79	3.48	2.29	1.04	
K_2O	n.d.	0.08	0.09	0.07	0.02	0.01	0.05	0.01	0.08	0.05	1.11	0.11	n.d.	0.01	0.02	0.57	n.d.	0.21	0.11	0.46	
P_2O_5	n.d.	n.d.	n.d.	n.d.	n.d.	n.d.	n.d.	n.d.	n.d.	n.d.	0.34	n.d.	n.d.	n.d.	n.d.	n.d.	n.d.	0.02	n.d.	0.01	
L.O.I.	7.72	2.30	2.01	1.38	5.85	3.81	1.20	0.89	1.80	1.17	1.96	0.32	5.67	7.96	3.97	1.27	1.71	1.96	1.83	1.25	
Total	99.97	99.95	99.98	99.91	99.93	99.94	99.93	100	99.98	99.93	99.91	99.96	99.91	99.96	99.92	99.93	99.92	99.78	99.92	99.98	
Mg#	86.0	84.3	82.0	82.6	87.6	87.1	84.5	84.4	85.0	84.2	55.0	80.0	93.6	87.8	86.5	89.3	85.9	77.7	82.0	54.1	
Zn	44	10	6	11	19	20	6	n.d.	9	6	73	14	n.d.	12	n.d.	n.d.	6	32	n.d.	47	
Cu	31	34	65	31	22	23	41	73	77	59	65	98	27	175	152	32	252	35	329	29	
Sc	9	10	17	14	n.d.	6	16	27	24	19	41	25	5	n.d.	n.d.	n.d.	36	33	18	46	
Ga	n.d.	n.d.	n.d.	n.d.	n.d.	5	5	5	n.d.	5	16	10	5	n.d.	3	10	9	n.d.	5	15	
Ni	1068	269	169	202	869	684	291	95	262	225	81	130	83	381	194	292	112	56	31	2	
Co	88	27	13	23	53	53	27	17	25	22	38	19	n.d.	57	30	10	14	25	9	30	
Cr	668	204	346	474	996	471	1107	413	1574	667	278	253	20	114	76	41	539	567	386	25	
V	29	34	67	54	11	17	54	105	93	70	287	91	n.d.	5	5	n.d.	108	185	62	776	
Rb	n.d.	n.d.	n.d.	n.d.	n.d.	n.d.	n.d.	n.d.	n.d.	n.d.	14	n.d.	n.d.	n.d.	n.d.	3	n.d.	n.d.	n.d.	n.d.	
Ba	n.d.	n.d.	12	11	n.d.	n.d.	7	6	10	n.d.	140	29	n.d.	n.d.	6	n.d.	n.d.	20	n.d.	98	
Nb	n.d.	n.d.	n.d.	n.d.	n.d.	n.d.	n.d.	n.d.	n.d.	n.d.	5	n.d.	n.d.	n.d.	n.d.	n.d.	n.d.	n.d.	n.d.	n.d.	
La	7	3	3	3	4	2	n.d.	n.d.	n.d.	3	6	4	11	n.d.	n.d.	4	10	3	n.d.	n.d.	
Sr	133	237	261	243	263	251	292	240	156	217	348	298	10	89	120	194	150	127	339	205	
Zr	8	10	12	11	11	13	13	12	11	11	134	17	2	6	5	5	6	25	9	14	
Y	2	3	4	3	2	2	3	5	4	4	39	6	1	1	1	n.d.	3	11	2	6	
Ti/Y	366	379	434	430	224	326	362	370	342	337	311	335	166	171	232		425	228	417	1158	
Zr/Y	4.95	3.62	3.21	3.46	7.13	6.14	4.16	2.64	2.72	3.23	3.44	2.85	2.65	4.50	4.04		2.25	2.33	4.28	2.38	

	K316	K103	K30
	gb	gb	Fe-gb
	isot	isot	isot
ICP-MS analyses:			
Rb	12.9	0.356	0.451
Sr	350	127	200
Y	37.7	9.56	4.69
Zr	131	21.5	12.5
La	6.89	0.986	1.63
Ce	19.8	2.58	3.73
Pr	3.30	0.401	0.463
Nd	16.1	2.00	1.98
Sm	5.07	0.678	0.602
Eu	1.70	0.211	0.311
Gd	5.73	0.815	0.739
Tb	1.03	0.148	0.127
Dy	6.79	1.02	0.849
Ho	1.48	0.219	0.177
Er	4.06	0.604	0.487
Tm	0.590	0.089	0.070
Yb	3.85	0.589	0.445
Lu	0.564	0.086	0.065
Nb	6.21	0.846	0.486
Hf	2.61	0.607	0.416
Ta	0.279	0.081	0.048
Th	0.184	0.143	0.083
U	0.068	0.049	0.113
Ta/Yb	0.07	0.14	0.11
Th/Yb	0.05	0.24	0.19
Th/Ta	0.66	1.77	1.74
Th/Tb	0.18	0.96	0.65
Ce/Y	0.51	0.24	0.62
Zr/Nb	21.6	29.1	29.7
Nb/Yb	1.61	1.44	1.09
Ta/Hf	0.11	0.13	0.11
$(La/Sm)_N$	0.88	0.94	1.74
$(Sm/Yb)_N$	1.46	1.28	1.50
$(La/Yb)_N$	1.28	1.20	2.62

Abbreviations, H.Pa: Harsin-Paeinab; H.Mj: Harsin-Moradjan; S: Sahneh; wehrl: wehrlite; ol-gb: olivine-gabbro; gb: gabbro; troc: troctolite; di: diorite; Fe-gb: ferrogabbro; cum: cumulitic; isot: isotropic; n.d.: not detected. Mg# = 100xMg/(Mg+Fe). Fe_2O_3 = 0.15xFeO. Normalizing values for REE ratios are from Sun and McDonough (1989).

the cpx-rich harzburgites may imply that more than one earlier partial melting event must have occurred (Hébert and Laurent, 1990). In other words, a re-melting of an already depleted peridotite may have caused the strong Ti depletion in cpx-rich harzburgites. By contrast, the high Ti content in clinopyroxenes from gabbros suggests that they crystallized from primary magmas generated from mantle sources that did not undergo previous partial melting events.

Plagioclase

Representative analyses of preserved plagioclase from gabbroic rocks are presented in Table 5. They have a wide compositional range with the lowest anorthite content in the foliated olivine-gabbro K62A (An = 59.3-66.7%), whereas in the other rocks the anorthite content ranges from 67.4-76.9%). Plagioclases from the foliated olivine-gabbro K62A are also slightly zoned, with cores ~2% richer in anorthite than rims. Plagioclases from the other gabbros do not show any significant zoning. The overall variability is shown in Fig. 6, where the magmatic zoning between core and rim in sample K62A is also shown. In general, the anorthite content, together with the Mg# of clinopyroxenes, is similar to that of MOR-type gabbros (Ross and Elthon, 1993). An high anorthite content is commonly related to the crystallization of plagioclase from water-rich magmas, whereas low anorthite plagioclase usually forms from water-poor magmas (e.g., Sisson and Grove, 1993). Therefore, plagioclases from the Kermanshah gabbros are likely to have been derived from a liquid, which crystallized at low H_2O content.

GEOCHEMISTRY

The geochemical features of the Kermanshah rocks are described using those major and trace elements, which are virtually immobile during low-temperature alteration and metamorphism (see Beccaluva et al., 1979; Pearce and Norry, 1979). They include some incompatible trace elements (e.g., Ti, P, Zr, Y, Sc, Nb, Ta, Hf, Th), middle (M-) and heavy (H-) REE, as well as some transition metals (e.g., Ni, Co, Cr, V). Large ion lithophile elements (LILE) are commonly mobilized during alteration. Nonetheless, when observing the relative variation of Ba and Rb with respect to Mg# and Zr, appreciable amounts of mobilization have been recognized only in a few samples, while in most of the studied rocks these elements show fairly good correlations with Zr and Mg# (not shown in this paper). Therefore, though with caution, these elements will also be used. When compared to immobile elements (e.g., Zr, Y), SiO_2, Al_2O_3, FeO, and CaO contents show fairly good correlations (not shown), suggesting that they have been moderately affected by alteration processes and therefore can be used. It should be noted that CaO content in the studied samples has been corrected by subtracting the CaO included in secondary calcite to the CaO content determined by XRF. More specifically, CaO in calcite has been calculated according to stoichiometric proportions with CO_2 contents. CO_2 has, in turn, been determined using a simple volumetric technique (Jackson, 1958). This simple correction has been possible since the petrographic analyses revealed that calcite is the only carbonate phase in the studied samples. Light REE (LREE) may also be affected by some extent of mobilization during alteration. However, the close correlation between these elements and many immobile elements (not shown) indicate that LREE have not been mobilized during the alteration processes.

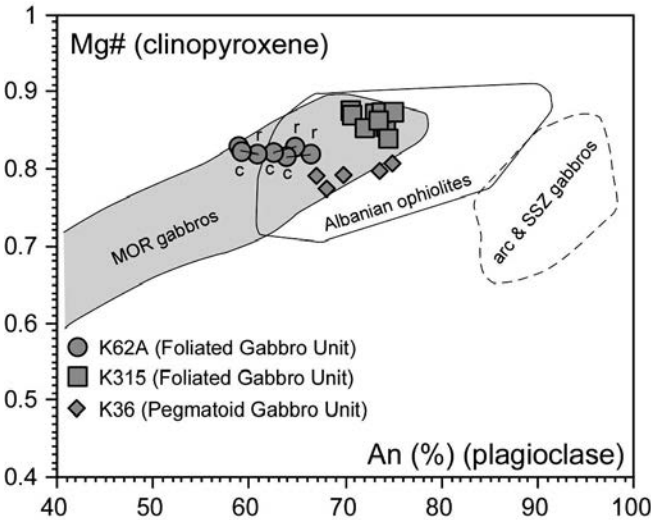

Fig. 6 - Anorthite (plagioclase) vs. Mg# (clinopyroxene) diagram for mafic intrusive rocks from the Kermanshah ophiolitic complex. Abbreviations, c: core; r: rim. The compositional variation for mid-ocean ridge (MOR) gabbros (Ross and Elthon, 1993), arc and supra-subduction zone (SSZ) gabbros (Burns, 1985), and Albanian ophiolite gabbros (Koller et al., 2006) are reported for comparison.

Mantle peridotites

The whole-rock major and trace element composition of mantle peridotites is presented in Table 6, while the variation of key elements vs. Mg# is shown in Fig. 7. All mantle peridotites have very low contents of TiO_2, P_2O_5, Zr, Y and high contents of Mg#, Ni, Cr (Table 6, Fig. 7). In terms of major elements, lherzolites, harzburgites, and dunites can be distinguished on the basis of TiO_2, Al_2O_3 and CaO contents, although these elements are very low in all rock types (Table 6). Accordingly, CaO content, although relatively variable, generally decreases from lherzolites to harzburgites and dunites. N-MORB-normalized incompatible element patterns and chondrite-normalized REE patterns are shown in Fig. 8. In general, Kermanshah mantle peridotites show a depletion in incompatible element concentrations with respect to the depleted MORB mantle of Workman and Hart (2005). All mantle peridotites have comparable LILE contents, which most likely reflect alteration. By contrast, lherzolites have high field strength element (HFSE) contents higher than those of harzburgites and dunites (Fig. 8a). Accordingly, lherzolites have MREE and HREE contents higher than those of harzburgites and dunites. Moreover, lherzolites display LREE depletion with respect to MREE and HREE (Ce_N/Sm_N = 0.05-0.86; Ce_N/Yb_N = 0.01-0.09), though lherzolite K1 displays a relative enrichment in La and Ce (Fig. 8b). Harzburgites and dunites are characterized by marked U-shaped chondrite-normalized patterns (Fig. 8b), that is, by a significant depletion in MREE with respect to LREE (La_N/Sm_N = 3.69-6.02) and HREE (Sm_N/Yb_N = 0.07-0.50). LREE concentration in these rocks is generally higher than in lherzolites. Regardless of the rock type, the Kermanshah mantle peridotites show REE depletion with respect to the depleted MORB mantle. In the Yb_N vs. Al_2O_3/SiO_2 diagram of Fig. 9a (where the Al_2O_3/SiO_2 decreasing ratio represents the increasing degree of depletion), all peridotite varieties show good correlation, which implies a strong interrelationship between HREE content and the

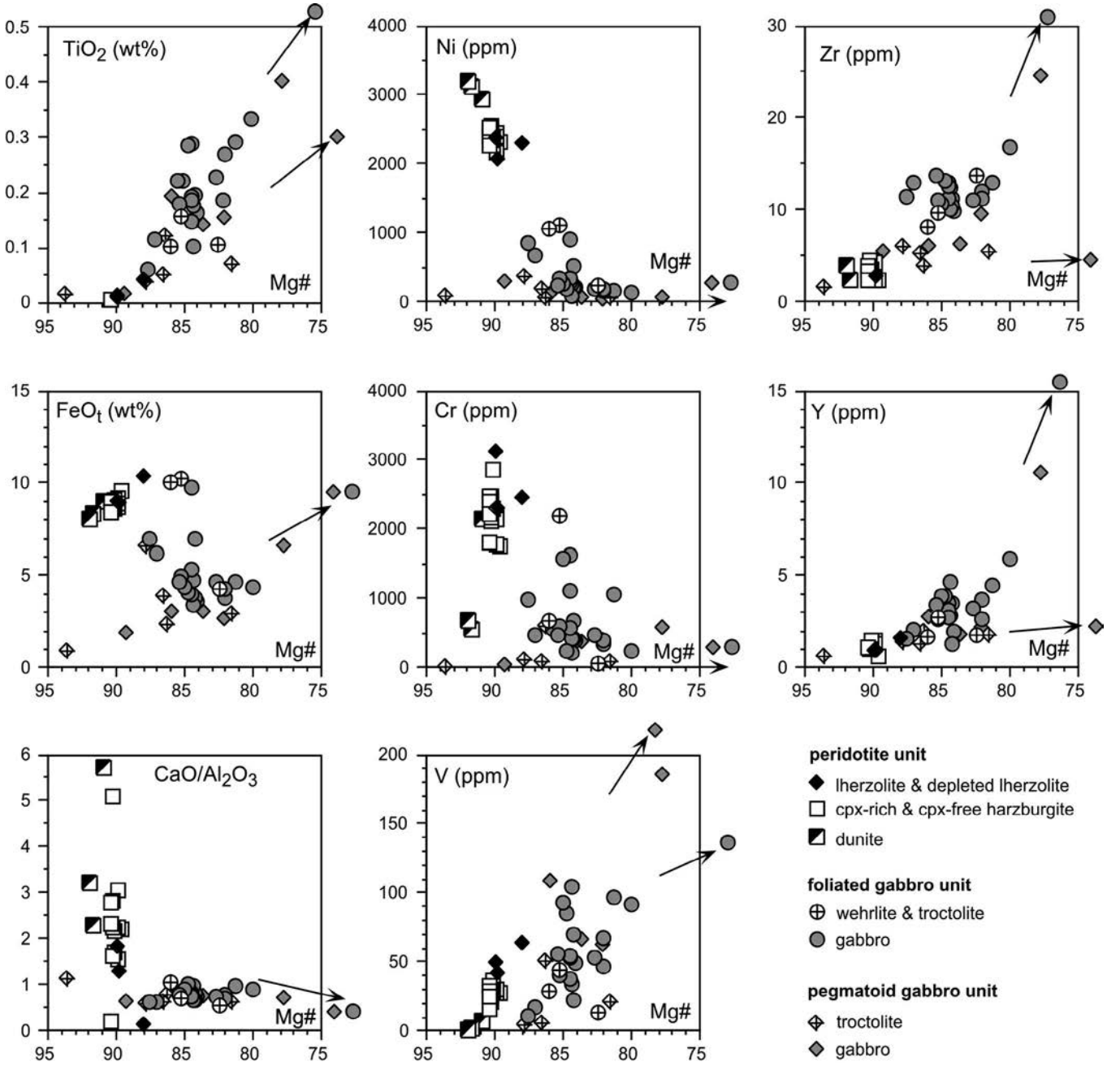

Fig. 7 - Variation of selected major and trace elements vs. Mg# [Mg# = molar Mg/(Mg+Fe)x100] for mantle peridotites, ultramafic and mafic rocks from the Kermanshah ophiolitic complex. For graphical reasons, only the more primitive compositions are plotted. The variation trends for the few differentiated rocks of each gabbro unit are indicated with arrows and relative symbols outside the panels. Major element oxides are recalculated on anhydrous bases.

composition of the whole rock. In Fig. 9b, the $(La/Sm)_N$ ratio correlates well with the degree of depletion, showing that the more depleted samples have a higher enrichment in LREE relative to MREE. When compared with the well-studied peridotites of the central Mediterranean area, the mantle peridotite varieties from Kermanshah show many similarities with equivalent rocks from the Dinaride Belt, as exemplified in Fig. 10.

Gabbroic rocks and associated mafic-ultramafic rocks

As described in the previous chapters, two different crustal facies can be recognized in the Kermanshah ophiolites (Fig. 3): (1) a Foliated Gabbro Unit consisting of wehrlites, troctolites, cumulate olivine-gabbros, and very rare isotropic gabbros; (2) a Pegmatoid gabbro unit consisting of troctolites, cumulate olivine-gabbros, gabbros, and rare Fe-gabbros. Representative whole-rock major and trace element compositions of these rocks are presented in Table 7; the variation of selected elements vs. Mg# is shown in Fig. 7.

Wehrlites display quite uniform compositions for many elements (e.g., SiO_2, Al_2O_3, Ni, Zr), with the exception of Cr (Table 7). By contrast, troctolites are rather variable in composition (Table 7), depending on the modal amount of cumulus and intercumulus phases. The largest elemental variations are observed (Table 7, Fig. 7) for Al_2O_3, MgO, CaO, Ni, and Cr, whereas all samples have very low contents of incompatible elements (e.g., TiO_2, P_2O_5, Zr, Y). Mg# is always high, ranging from 93.6 to 81.5.

Gabbroic rocks from the Foliated Gabbro Unit include olivine-gabbros and gabbros. In terms of major elements, no significant compositional difference can be observed between olivine-gabbros and gabbros (Table 7). Mg# is generally high (80.0-87.6), with the exception of sample K316, which has Mg# = 55.0 (Fig. 7). This suggests that most of the gabbros from the Foliated Gabbro Unit represent rather primitive rocks, which are also characterized by very low contents of TiO_2, P_2O_5, Zr, and Y. Al_2O_3, CaO, and MgO contents are very variable (Table 7). This variability correlates well with the modal amounts of olivine, plagioclase, and clinopyroxene. The Al_2O_3 geochemical behaviour reflects the large amount of plagioclase crystallization and is negatively correlated with MgO. MgO concentrations largely reflect the abundance of modal olivine. Accordingly, Ni and Cr contents are also very variable (Table 7). The most evolved isotropic gabbro K316 has high contents TiO_2, P_2O_5, Zr, Y, and V, while Al_2O_3, MgO, Ni, and Cr are relatively low. This sample is assumed to be representative of a magma composition and displays a quite flat N-MORB normalized incompatible element pattern, with most element concentrations ranging from 1 to 3 times N-MORB (Fig. 11a). Chondrite-normalized REE composition (Fig. 11b) shows a slight LREE/HREE enrichment (La_N/Yb_N = 1.28) coupled with a slight LREE/MREE depletion (La_N/Sm_N = 0.88). The incompatible element and REE composition of this gabbro is similar to those of gabbros generated in a mid-ocean ridge setting. REE composition (Fig. 11b) and many incompatible element ratios (e.g., Ta/Yb, Th/Yb, Ce/Y, Zr/Nb, Table 7) indicate that this isotropic gabbro is geochemically similar to N-MORBs.

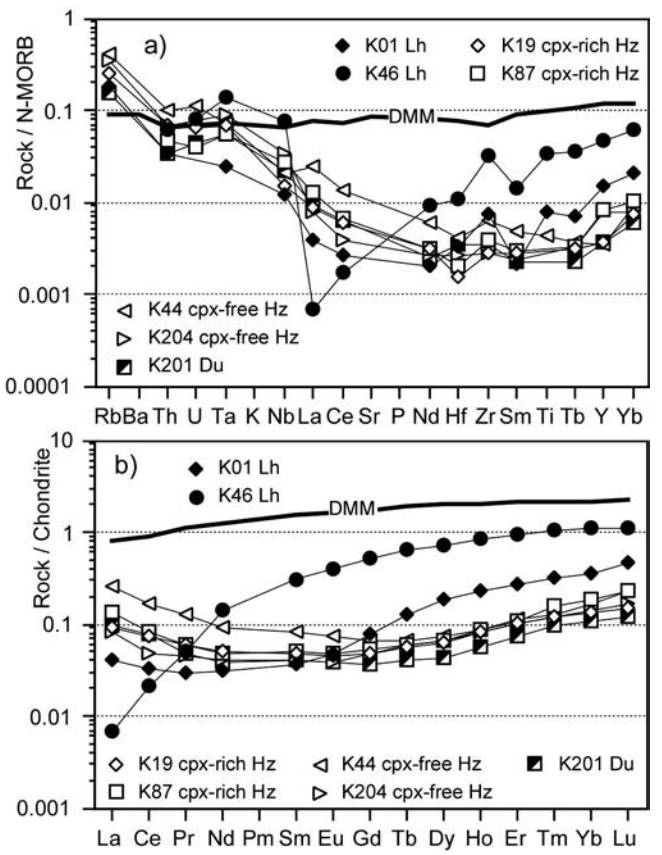

Fig. 8 - N-MORB normalized incompatible element patterns (a) and chondrite-normalized REE patterns (b) for mantle peridotites from the Kermanshah ophiolitic complex. Normalizing values are from Sun and McDonough (1989). Abbreviations, Lh: lherzolite; Cpx-Hz: clinopyroxene-rich harzburgite; Hz: clinopyroxene-free harzburgite; Du: dunite. The composition of the depleted MORB mantle (DMM) of Workman and Hart (2005) is shown for comparison.

Gabbroic rocks from the Pegmatoid Gabbro Unit include cumulitic olivine-gabbros, gabbros and very rare isotropic ferrogabbros and diorites. Mg# is generally high (82.0-89.3). They are characterized by very low contents of TiO_2 (<0.19wt%) P_2O_5 (below detection limit), Zr (5-9 ppm), and Y (2-3 ppm). The incompatible element contents are generally lower than those observed in the foliated gabbros (Fig. 7). Al_2O_3 content is very variable (16.96-26.87wt%), whereas the variation in CaO and MgO contents is moderate (Table 7). Accordingly, Ni and Cr contents are also very variable and range from 31 to 292 ppm and from 41 to 539 ppm, respectively. Moreover, these elements are generally lower than in the foliated gabbros (Fig. 7). The diorite K103 has comparatively higher values of incompatible elements and MgO and a comparatively lower content of Al_2O_3, whereas the transition metal contents are comparable to those of gabbroic rocks (Table 7). The ferrogabbro K30 is characterized by high TiO_2, FeO_t, and V (Table 7). Both ferrogabbro and diorite are slightly enriched in LILE with respect to HFSE (Fig. 11a). However, while the diorite has a rather flat chondrite-normalized REE pattern, the ferrogabbro displays a marked LREE/HREE enrichment (Fig. 11b).

Although the ferrogabbro and diorite display different REE patterns, they have very similar incompatible element ratios (e.g., Ta/Yb, Th/Yb, Th/Ta, Zr/Nb, Ta/Hf, Table 7), which suggest that these two rocks shared a common parental magma. The difference in REE patterns is therefore most likely related to different stages of fractionation. Moreover, the LILE/HFSE slightly enriched incompatible element patterns (Fig. 11a) and the incompatible element ratios indicate that these rocks are geochemically similar to enriched-type MORBs (E-MORBs).

DISCUSSION

Petrogenesis and tectono-magmatic significance of mantle peridotites

From the petrographic observations, mineral chemistry and whole-rock chemical data presented in the previous chapters can be seen that Kermanshah mantle tectonites are represented by variably depleted peridotites, which range from depleted lherzolite to very depleted harzburgite. Some features are particularly noteworthy: (1) the very depleted nature of harzburgites; (2) the generally high LREE/MREE enrichment in harzburgites; (3) the strong LREE/HREE depletion in the lherzolite K46 (Fig. 7); (4) a significant LREE enrichment in the lherzolite K1.

Depleted mantle peridotites exposed in ophiolitic massifs are commonly considered as residual mantle lithosphere that underwent extraction of MORB and/or SSZ melts. In particular, depleted lherzolites commonly represent a residual MORB mantle, while depleted harzburgites represent a residual SSZ mantle (e.g., Saccani et al., 2004; 2008, and reference therein). Therefore, in order to test the hypothesis that the Kermanshah depleted lherzolites may represent mantle residua after MORB-melt extraction, a non-modal, batch partial melting modelling of a depleted MORB-type asthenospheric source is presented in Fig. 12a. A rigorous quantification of the melting processes is not possible as the composition of the mantle source is difficult to constrain. However, a semi-quantitative modelling of the REE can

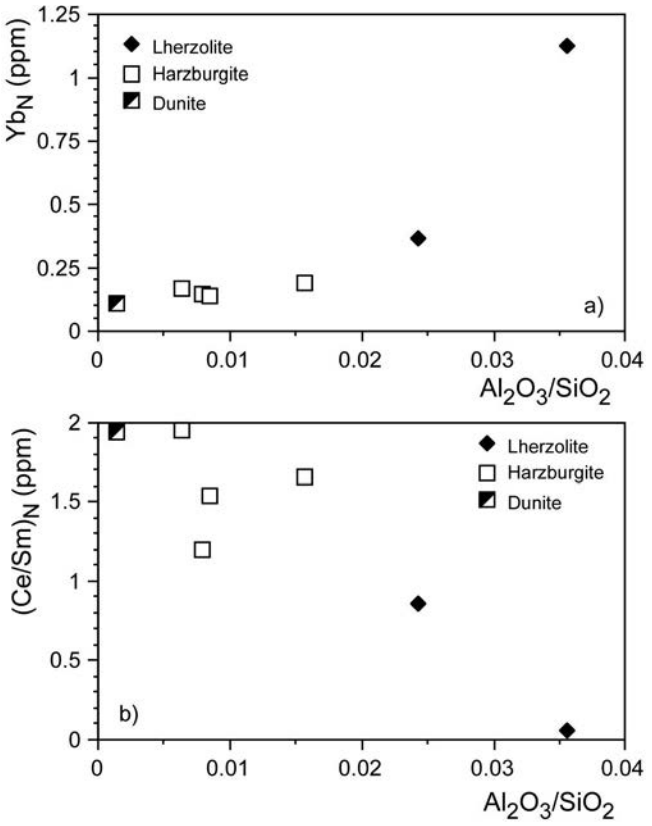

Fig. 9 - Whole rock $(Yb)_N$ (a) and $(Ce/Sm)_N$ (b) vs. Al_2O_3/SiO_2 diagrams for mantle peridotites from the Kermanshah ophiolitic complex. Normalizing values are from Sun and McDonough (1989).

place some effective constraints on the abovementioned hypothesis. The depleted MORB mantle (DMM) of Workman and Hart (2005) is assumed as the possible mantle source in Fig. 12a. The modal composition (olivine = 53%, orthopyroxene = 27%, clinopyroxene = 17%, spinel = 3%) and melting proportions (olivine = -0.06, orthopyroxene = 0.28, clinopyroxene = 0.67, spinel = 0.11) are from Workman and Hart (2005) and Kinzler (1997), respectively. The REE distribution coefficients are from Frey (1969). It can be observed in Fig. 12a that the chondrite-normalized-REE pattern of the depleted lherzolite K46 is compatible with the calculated residual compositions after 15-20% partial melting of the DMM source. It can therefore be postulated that Kermanshah depleted lherzolites may represent the oceanic mantle residuum after MORB-melt extraction. Accordingly, the Cr# in spinels and Mg# in olivine (Fig. 13) indicate that these lherzolites may represent mantle residua after 10-12% melt extraction.

Low concentrations of incompatible elements and relative enrichment in HFSE and LREE in mantle peridotites are commonly interpreted as the result of previous melt removal and subsequent enrichment in LREE (e.g., Hickey and Frey, 1982). Both cpx-rich and cpx-free harzburgites are characterized by very low concentrations of incompatible elements and REE, but show significant LILE/HFSE and LREE/MREE enrichments (Fig. 8). Such geochemical features are typically observed in many SSZ ophiolitic counterparts, (e.g., in the Hellenides, Saccani et al., 2004; Barth et al., 2008; in East Iran, Saccani et al., 2010), as well as in modern SSZ oceanic settings (e.g., Hickey and Frey, 1982; Pearce et al., 1992; 2000) and are interpreted as the result of boninitic-type melt removal in SSZ settings (Hickey and Frey, 1982; Pearce et al., 1992; Saccani et al., 2004; Barth et al., 2008). The mantle source required for the production of boninite-type melts corresponds to a residual MORB mantle, which was subsequently enriched in LILE and LREE by subduction-derived hydrous fluids (Hickey and Frey, 1982; Pearce et al., 1992; 2000). In order to test the hypothesis that Kermanshah harzburgites may represent residual mantle after extraction of SSZ magmas, a semi-quantitative REE modelling is presented in Fig. 12b. A depleted, LREE/MREE enriched lherzolite from the Nehbandan ophiolites (Sistan Suture Zone, E Iran) was assumed to be the mantle source. Saccani et al. (2010) demonstrated that this depleted lherzolite represent a residual mantle after 10-15% MORB melt extraction, which was subsequently enriched in LREE by subduction-derived fluids. The modal composition (olivine = 71%, orthopyroxene = 24%, clinopyroxene = 4%, spinel = 1%) and melting proportions (olivine = 0.09, orthopyroxene = 0.64, clinopyroxene = 0.24, spinel = 0.02) are from Kostopoulos and Murton (1992). The REE distribution coefficients for La to Dy are from McKenzie and O'Nions (1991) and for Ho to Lu are from Fujimaki et al. (1984). Calculated melts for 10-30% fractional partial melting of the assumed source correspond to typical boninitic melts (e.g., Hickey and Frey, 1982; Beccaluva and Serri, 1988). The associated calculated mantle residua after 25-30% partial melt extraction fit the compositions of some depleted harzburgites from the Kermanshah ophiolites (Fig. 12b). It can therefore be concluded that LREE/MREE enriched cpx-rich harzburgites may represent the mantle residua of a SSZ magmatism. This conclusion is also supported by the Cr# in spinels plotted against Mg# in olivine in Fig. 13. Cr-spinel and olivine in the various harzburgite types have refractory compositions, which are compatible with 20-30% partial melt extraction.

It should finally be noted that the REE composition of lherzolite K46 is identical from Eu to Lu to the depleted lherzolite assumed as the mantle source. This implies that the depleted lherzolites representing residual MORB mantle were subsequently trapped in a SSZ mantle wedge and enriched in LREE by subduction-derived fluids. The relative enrichment in La and Ce with respect to Sm observed in lherzolite K1, further supports this conclusion. The maximum extent of LREE enrichment that the residual MORB mantle experienced in the SSZ setting can empirically be estimated by observing the LREE enrichment of the assumed mantle source with respect to the LREE/MREE depleted lherzolite K46 (Fig. 12b).

Petrogenesis and tectono-magmatic significance of gabbroic rocks and associated mafic-ultramafic rocks

Rocks from the crustal ophiolitic sequences define a general trend, which is consistent with the progressive removal of cumulate phases from the magma. The overall differentiation trend is from highly magnesian ultramafic cumulates to cumulate and isotropic gabbros, ferrogabbros and diorites (Fig. 7). The CaO/Al_2O_3 ratios are almost constant when Mg# decreases from 94 to ~75 and show a smooth decrease for Mg# <~ 75 (Fig. 7). According to petrographic observations, such a trend in CaO/Al_2O_3 ratios reflects the earlier crystallization of plagioclase followed by the crystallization of plagioclase and clinopyroxene. The Ni and Cr contents decrease with decreasing Mg#, consistent with the fractionation of olivine and Cr-spinel. However, the decrease of these elements in rocks of the Pegmatoid Gabbro Unit is

much smoother then in their counterparts from the Foliated Gabbro Unit. The FeO_t and V contents increase with decreasing Mg#, consistent with later fractionation of clinopyroxene and Fe-Ti oxides. Zr and Y sharply increase with decreasing Mg# in Foliated Gabbro Unit rocks, whereas they smoothly increase in rocks from the Pegmatoid Gabbro Unit. These overall geochemical features indicate that rocks from both Foliated and Pegmatoid Gabbro Units were generated in a mid-ocean ridge setting. However, the incompatible element and REE compositions of the few samples that most likely represent liquid compositions (i.e., non cumulitic rocks), indicate that the isotropic rocks from the Foliated Gabbro Unit and those from the Pegmatoid Gabbro Unit may have been generated from compositionally slightly different parental magmas. The LREE/MREE depletion ($La_N/Sm_N = 0.88$) indicates that the isotropic foliated gabbro may have formed from parental magma with N-MORB composition. Many incompatible element ratios (e.g., Ta/Yb, Th/Yb, Ce/Y, Zr/Nb, Table 7), which are included in the typical range for N-MORBs, further support this conclusion. Accordingly, when plotted in the most popular discrimination diagrams (e.g., Meschede, 1986; Wood, 1980) this gabbro plots in the fields for N-MORBs (not shown).

By contrast, when compared to the isotropic foliated gabbro, both ferrogabbro and diorite from the Pegmatoid Gabbro Unit are slightly enriched in LILE with respect to HFSE (Fig. 11a). Although the ferrogabbro and diorite from the Pegmatoid Gabbro Unit display different REE patterns, they have very similar incompatible element ratios (e.g., Ta/Yb, Th/Yb, Th/Ta, Zr/Nb, Ta/Hf, Table 7), which suggest that these two rocks shared a common parental magma. Moreover, the LILE/HFSE slightly enriched incompatible element patterns (Fig. 11a) and the incompatible element ratios (Table 7) indicate that these rocks are geochemically similar to E-MORBs. Accordingly, when plotted in different discrimination diagrams (e.g., Meschede, 1986; Wood, 1980) they plot in the fields for E-MORBs (not shown). These data indicate that rocks from the Pegmatoid Gabbro Unit may have formed from a slightly enriched parental magma.

It should however be taken into account that the relative LILE/HFSE enrichment observed in these rocks could either be explained by partial melting of a more enriched mantle source or, alternatively, by lower degrees of partial melting when compared to N-MORBs. An estimation of the composition of primary magmas and relative mantle sources can be obtained using hygromagmatophile element ratios (Allègre and Minster, 1978). In fact, the very different Th/Ta and Th/Tb ratios observed in gabbros from the Pegmatoid and Foliated Units (Table 7) suggest that these two gabbro series most likely represent melts derived from compositionally distinct mantle sources, rather than melts derived from different degrees of partial melting. In summary, the geochemical features suggest that both Pegmatoid and Foliated Units have most likely formed in a mid-ocean ridge setting, though gabbros from the Foliated and Pegmatoid Units probably derived from a depleted and a more enriched mantle sources, respectively.

Geodynamic implications

In this section we use the geochemical and petrogenetic characteristics of the Kermanshah ophiolites, in order to evaluate the nature and geodynamic significance of the magmatic events that occurred in the Arabian-Iranian sector of the Neo-Tethyan Ocean. Various hypotheses have been proposed in literature for the tectonic evolution of the Arabian-Iranian sector of the Neo-Tethyan Ocean and surrounding continental margins (Berberian and King, 1981; Desmons and Beccaluva, 1983; Dercourt et al., 1986; Lippard et al., 1986; Glennie, 2000; Stampfli et al., 2001; Golonka, 2004; Agard et al., 2005; Robertson, 2007). Nonetheless, they are basically similar but mostly differ in the timing of the events that occurred in this basin from Late Permian to Present. A schematized tectono-magmatic model that can explain the different rock associations included in the Kermanshah ophiolitic mélange is presented in Fig. 14. According to Stampfli et al. (2001), the continental breakup and the opening of this oceanic sector

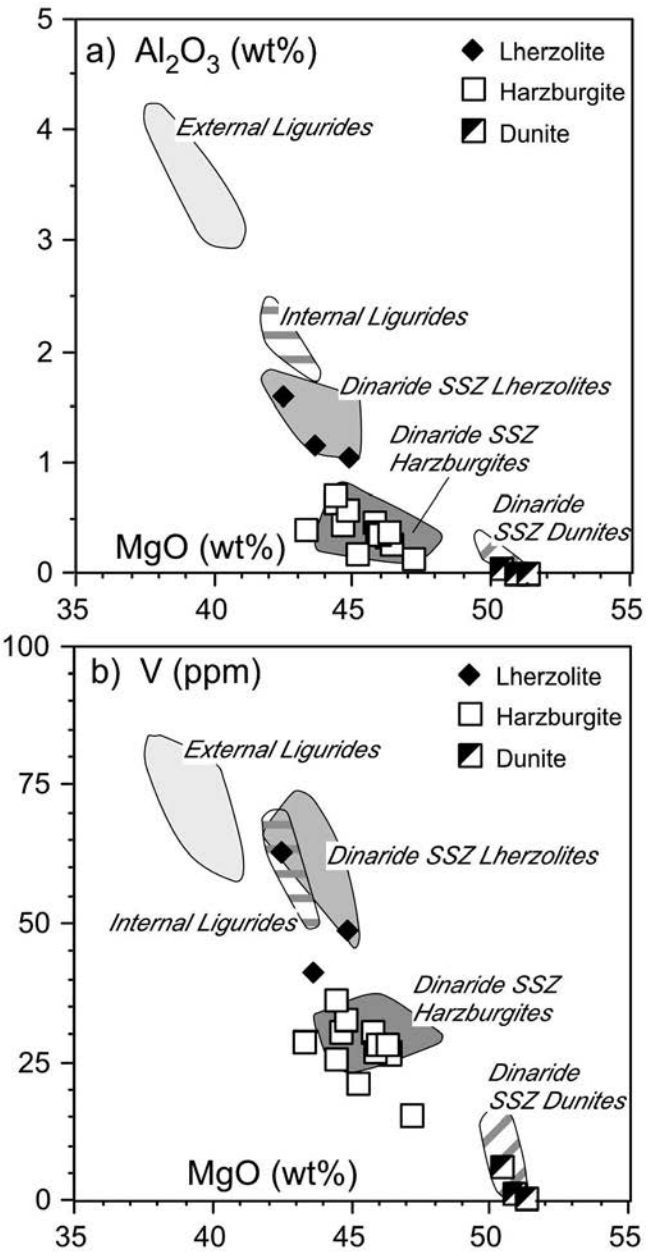

Fig. 10 - Variation of Al_2O_3 (a) and V (b) vs. MgO in mantle peridotites from the Kermanshah ophiolitic complex. Elemental variations in mantle peridotites from the Ligurides (N. Apennine belt) and the central-southern Dinaride belt (Albanides-Hellenides) are reported for comparison. Data source, External Ligurides: Rampone et al. (1995); Internal Ligurides: Rampone et al. (1998); Dinaride lherzolites and supra-subduction zone (SSZ) dunites: Beccaluva et al. (1994); Dinaride SSZ harzburgites: Saccani et al. (2004).

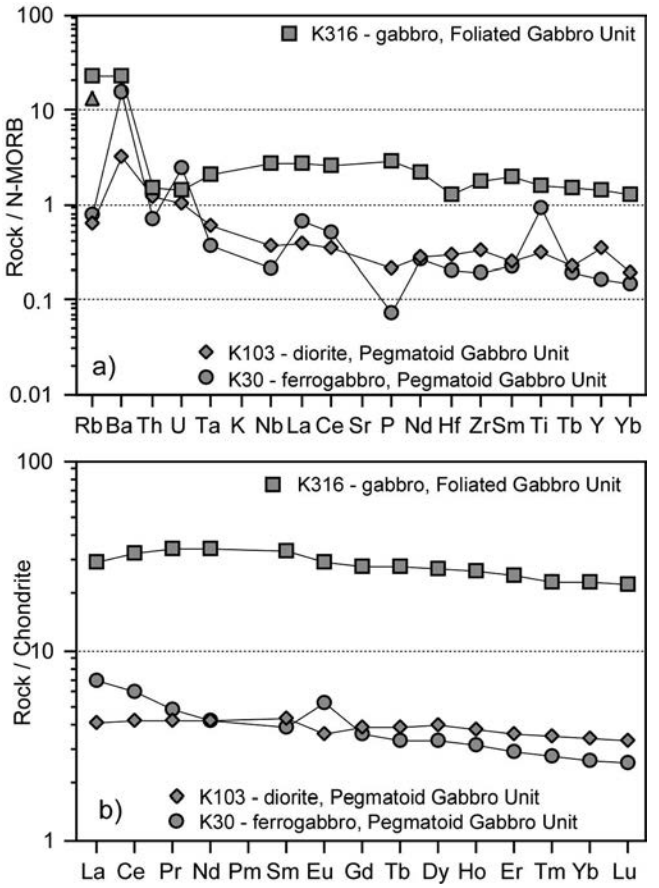

Fig. 11 - N-MORB normalized incompatible element patterns (a) and chondrite-normalized REE patterns (b) for gabbroic rocks from the Kermanshah ophiolitic complex. Normalizing values are from Sun and McDonough (1989).

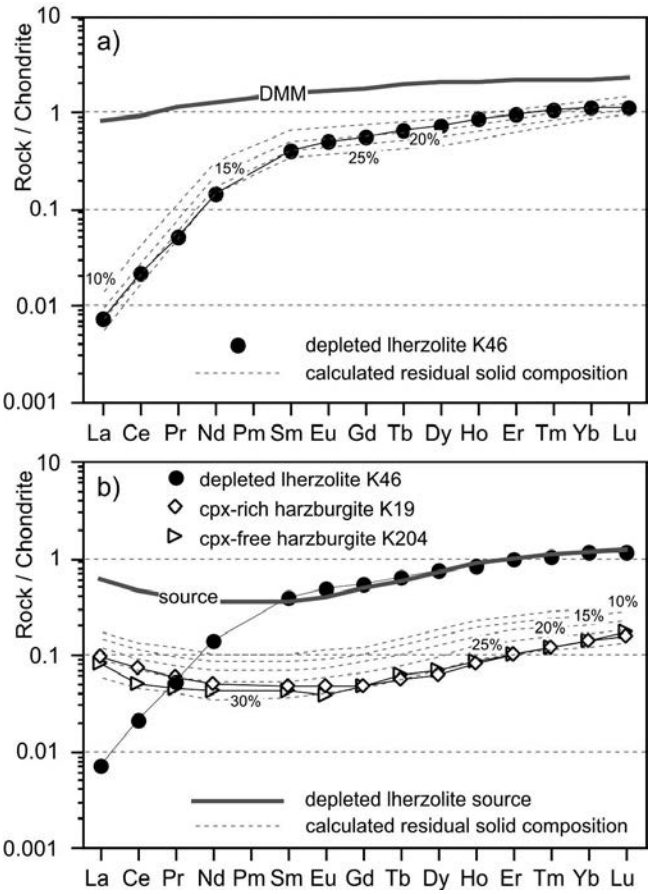

Fig. 12 - Calculated chondrite-normalized (Sun and McDonough, 1989) REE patterns for solid residua after various degrees of partial melting of: a) depleted MORB mantle (DMM) of Workman and Hart (2005); b) depleted lherzolite from the Nehbandan ophiolites, Sistan Suture Zone, E Iran (Saccani et al., 2010). The model assumes various degrees of partial melting according to non-modal batch melting. REE patterns of mantle peridotites from the Kermanshah ophiolitic complex are also reported.

occurred in Permian time, while Lippard et al. (1986) suggested a Triassic time for the opening phase. Whatever the age, the early stage of oceanization was characterized by the formation of enriched-type MORBs and alkaline WPBs (Lippard et al., 1986). In many interpretations (e.g., Dercourt et al., 1986; Agard et al., 2005), the northern continental margin of the Neo-Tethys is represented in this area by the Sanandaj-Sirjan zone (Fig. 1a). By contrast, Glennie (2000) suggested that the Sanandaj-Sirjan zone represents a continental fragment rifted from the conjugate, southern Oman margin and that Neo-Tethyan oceanic lithosphere separated the Sanandaj-Sirjan block from the Lut continental block to the north. However, Robertson (2007) observed that the available data do not allow a detailed correlation between Oman and the Sanandaj-Sirjan. All interpretations concur with the idea that in Late Triassic time the Arabian-Iranian Neo-Tethys had already reached its steady-state condition (Fig. 14a). According to some authors, the Neo-Tethyan oceanic lithosphere was consumed in a NE-dipping subduction beneath the Sanandaj-Sirjan continental margin during the Early Jurassic (Dercourt et al., 1986) or Middle Jurassic (Agard et al., 2005). At this time (Fig. 14b), the oceanic spreading was still active and was probably located to the south, close to the Arabian margin (Dercourt et al., 1986). These authors also suggested that the oceanic spreading persisted until Late Cretaceous time, as suggested by the occurrence of lower Late Cretaceous ophiolites in Oman and Iran (Delaloye and Desmons, 1980; Knipper et al., 1986).

The MORB signature displayed by the intrusive rocks of both Foliated and Pegmatoid Gabbro Units, indicates that they represent dismembered remnants of oceanic crust generated at a mid-ocean spreading ridge. Moreover, REE modelling (Fig. 12a) demonstrates that Kermanshah depleted lherzolites represent mantle residua after 15-20% extraction of normal-type MORB melts. Accordingly, the N-MORB signature of Foliated Gabbro Unit suggests that these rocks originate from primary melts, which in turn resulted from the partial melting of pure MORB-type mantle sources. Therefore, in the evolutionary framework of the Arabian-Iranian Neo-Tethys, the formation of both Kermanshah depleted lherzolites and foliated gabbros may be associated with the Triassic-Early Cretaceous oceanic spreading stage. The Kermanshah Pegmatoid Gabbro Unit displays an E-MORB signature and most likely originated from partial melting of a MORB-type mantle source enriched in LREE and LILE. Robertson (2007) suggested that enriched-type MORBs from the conjugate Oman ophiolites formed (together with alkaline WPBs) during the early stage of oceanic formation. In addition, Ghazi and Hassanipak (1999) reported the occurrence of volcanic rocks with alkaline WPB affinity in the Kermanshah ophiolites. Therefore, it can

reasonably be postulated that the Pegmatoid Gabbro Unit can be correlated with the E-MORBs of Oman and that they formed during the early oceanization phase.

Desmons and Beccaluva (1983) and Dercourt et al. (1986) suggested that, concomitant with the ceasing of see-floor spreading, a NE-dipping intra-oceanic subduction, located close to the northern margin of Arabia, was established in the Late Cretaceous. By contrast, Agard et al. (2005) suggested an Early Cretaceous age for the intra-oceanic subduction, which does not necessarily imply the concurrent ceasing of the see-floor spreading. The occurrence of typical SSZ ophiolites, such as depleted mantle harzburgites, further supports the hypothesis that the subduction was accompanied by the development of an intra-oceanic arc (Fig. 14c, d). In fact, the REE modelling shown in Fig. 12b demonstrates that Kermanshah harzburgites may represent the residual mantle after extraction of 25-30% of boninitic-type melts. The data presented herein show that all harzburgites have LREE/MREE enrichment typical of mantle peridotites metasomatized by SSZ fluids. Consistent with the model proposed by many authors for the genesis of boninitic rocks in intra-oceanic settings (e.g., Stern et al., 1991), the magmatism in the SSZ was most likely associated with upwelling and decompressional melting of a depleted, residual MORB mantle, which was enriched in LREE by fluids derived from the dehydration of the sinking slab (Fig. 14c). Such a mantle upwelling was associated with extending movements in the forearc region. Though boninitic-type volcanic rocks are not found in the Kermanshah ophiolites, Desmons and Beccaluva (1983) reported the occurrence of low-Ti basaltic dykes, typical of SSZ settings. Many reasons can explain the absence of SSZ-type volcanic rocks in the Kermanshah area. The simplest one is that they underwent erosional processes. However, the very limited occurrence in the Kermanshah mélange of crustal rocks coupled with the prevalent occurrence of SSZ mantle rocks may suggest that different portions of the SSZ lithosphere were selectively incorporated into the accretionary prism. In fact, hot and highly depleted residual mantle is significantly more buoyant than a more fertile mantle, and may be effectively trapped within the wedge corner (Fig. 14d). As a consequence, the SSZ depleted mantle trapped in the wedge corner could be included into the accretionary prism with respect to the arc crust. By contrast, partial sections of the oceanic crust may effectively be tectonically incorporated in the lower part of the accretionary prism (Fig. 14). These may explain the occurrence in the Kermanshah mélange of incomplete oceanic crustal portions tectonically overlain by SSZ mantle peridotites.

According to Lippard et al. (1986) and Robertson (1987), the intra-oceanic subduction persisted until the trench collided with the northern margin of Arabia in Late Cretaceous time (Fig. 14e). By then, ophiolites were emplaced onto the Arabian continental margin. Stratigraphic evidence suggests, in fact, that the Kermanshah mélange formed in Late Cretaceous time and it was soon after emplaced onto the Arabian continental margin (Delaloye and Desmons, 1980).

After the Late Cretaceuos, the magmatic activity continued on the southern, “Andean-type” margin of the Sanandaj-Sirjan block with the production of calc-alkaline and alkaline volcanic and plutonic rocks, which peaked in the Eocene (Berberian and King, 1981; Leterrier, 1985). The continental collision caused the tectonic emplacement of these Eocene rocks onto the ophiolitic sequences (Fig. 14f).

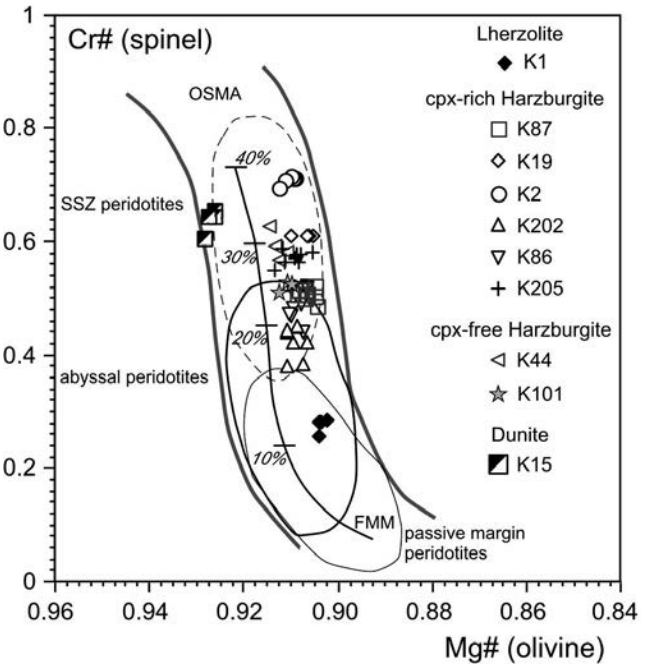

Fig. 13 - Cr#(spinel) vs. Mg# (olivine) diagram for mantle peridotites of the Kermanshah ophiolitic complex. The olivine–spinel mantle array (OSMA) and melting trend of Arai (1994). FMM= fertile MORB mantle. Compositional variations for abyssal peridotites are from Dick and Bullen (1984); compositional variations for oceanic supra-subduction zone and passive continental margin peridotites are from Pearce et al. (2000).

CONCLUSION

The data presented in this paper indicate that the Kermanshah ophiolites consist of various, dismembered ophiolitic sequences that record different Mesozoic evolutionary stages of the Arabian-Iranian branch of Neo-Tethys. These ophiolitic sequences include rocks generated in a mid-ocean ridge setting, such as: (1) depleted mantle lherzolites; (2) a troctolite, cumulate gabbro, isotropic gabbro sequence mainly showing pegmatoid texture; (3) a wehrlite, cumulate gabbro, isotropic gabbro sequence showing foliated texture. The crustal rocks show the typical MORB-type petrographic, mineralogical, and geochemical characteristics, while REE modelling shows that depleted lherzolites have MREE and HREE abundance similar to that of residual MORB mantle, which experienced 15-20% removal of MORB melts. In addition, gabbros from the Pegmatoid Unit show E-MORB chemical signature, whereas foliated gabbros have N-MORB chemical features.

However, the volumetrically most abundant ophiolitic variety in the Kermanshah area is represented by mantle rocks generated in an intra-oceanic arc setting. They consist of depleted and very depleted harzburgites and dunites. REE modelling shows that harzburgites have REE compositions similar to that of residual SSZ mantle, which experienced 25-30% removal of boninitic melts. In addition, their significant LREE/MREE enrichment suggests that these rocks represent SSZ mantle enriched in LREE by fluids released from the subducting slab.

The generation of these different ophiolitic units can be framed in the current geodynamic interpretations of the Arabian-Iranian Neo-Tethys. Depleted lherzolites and both gabbroic units have been formed during the Triassic-Cretaceous oceanic spreading stage of the Arabian-Iranian Neo-Tethys.

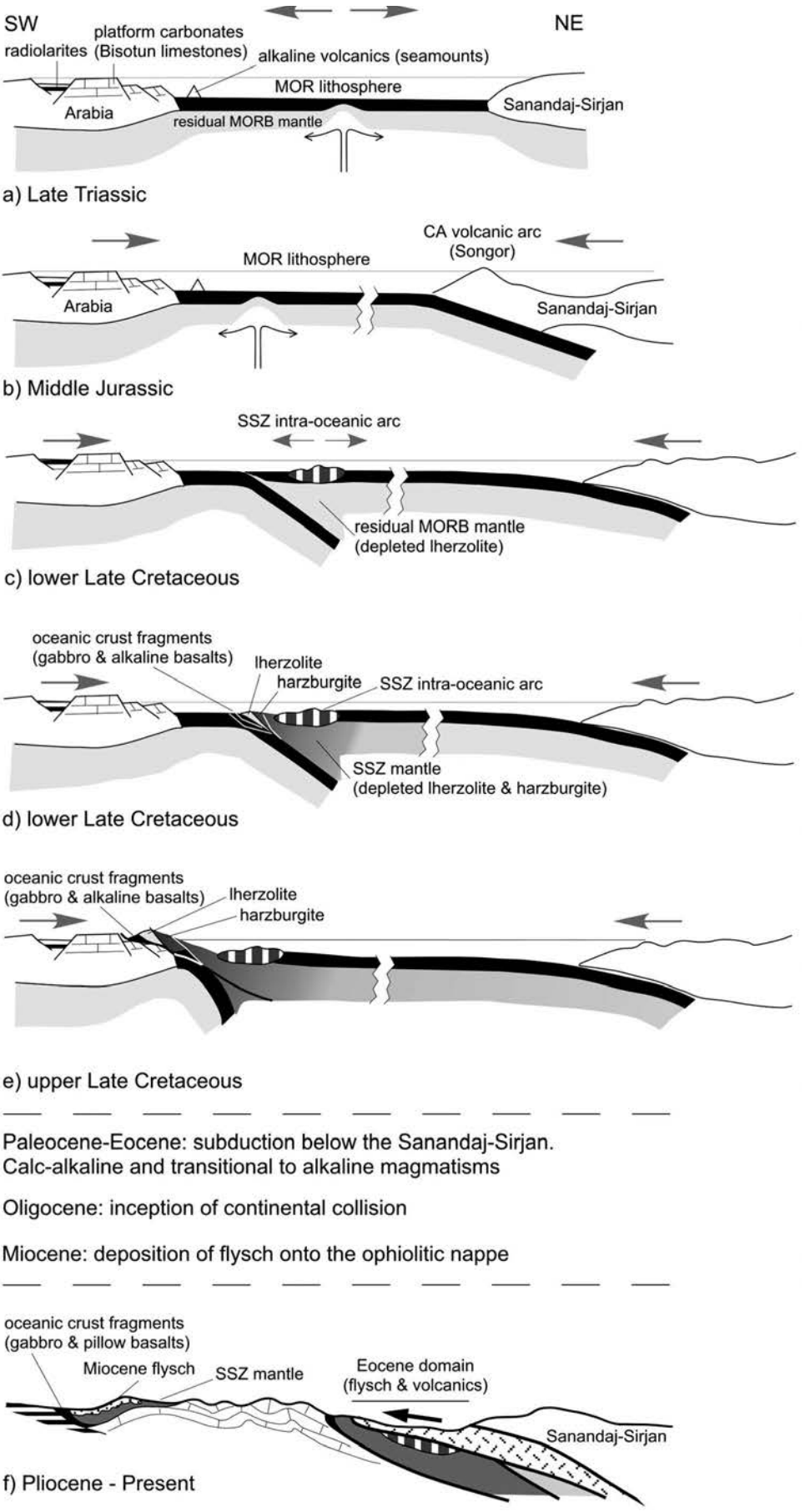

Fig. 14 - 2-D cartoon (not to scale) showing the tectono-magmatic evolution proposed for the Kermanshah ophiolites and surrounding areas. Loosely based on Desmons and Beccaluva (1983), Dercourt et al. (1986) and Agard et al. (2005). Ages are by no means conclusive.

Nonetheless, the E-MORB signature of Pegmatoid Gabbro Unit accounts for a genesis from a mantle source enriched in LREE and LILE that can be associated with the early stage of oceanic spreading (Robertson, 2007). By contrast, harzburgites can be associated with the Cretaceous intra-oceanic arc stage postulated by several authors (e.g., Desmons and Beccaluva, 1983; Dercourt et al., 1986; Agard et al., 2005).

ACKNOWLEDGMENTS

This paper is the result of the PhD project of K. Allahyari. The Iranian ministry of Science, Research and Technology and the Italian Ministry of University are acknowledged for the financial support. Special thanks go to the staff of the Dipartimento di Scienze della Terra, Università di Ferrara, Italy; in particular, R. Tassinari is gratefully acknowledged for his support with analytical techniques. Many thanks go to R. Carampin and A. Fioretti (CNR, Padua) for their support with EPMA analyses. We also thank S. Arai for his constructive review of this paper and R. Tribuzio for his useful suggestions.

REFERENCES

Agard P., Omrani L., Jolivet L. and Mouthereau F., 2005. Convergence history across Zagros (Iran): constraints from collisional and earlier deformation. Int. J. Earth Sci. (Geol. Rundsch.), 94: 401-419. DOI 10.1007/s00531-005-0481-4.

Alavi M., 1994. Tectonics of the Zagros orogenic belt of Iran: new data and interpretations. Tectonophysics, 229: 211-238.

Allègre C.J. and Minster J.F., 1978. Quantitative models of trace element behavior in magmatic processes. Earth Planet. Sci. Lett., 38: 1-25.

Arai S., 1994. Characterisation of spinel peridotites by olivine–spinel compositional relationships: review and interpretation. Chem. Geol., 113: 191-204.

Barth M.G., Mason, P.R.D., Davies G.R. and Drury M.R., 2008. The Othris ophiolite (Greece): A snapshot of subduction initiation at a mid-ocean ridge. Lithos, 100: 234-254.

Beccaluva L., Coltorti M., Premti I., Saccani E., Siena F. and Zeda O., 1994. Mid-Ocean Ridge and Suprasubduction affinities in the Ophilitic Belts from Albania. Ofioliti, 19: 77-96.

Beccaluva L., Di Girolamo P., Macciotta G. and Morra V., 1983. Magma affinities and fractionation trends in ophiolites. Ofioliti, 8: 307-324.

Beccaluva L., Ohnenstetter D. and Ohnenstetter M., 1979. Geochemical discrimination between ocean-floor and island-arc tholeiites-application to some ophiolites. Can. J. Earth Sci., 16: 1874-1882.

Beccaluva L. and Serri G., 1988. Boninitic and low-Ti subduction-related lavas from intraoceanic arc-backarc systems and low-Ti ophiolites: a reappraisal of their petrogenesis and original tectonic setting. Tectonophysics, 146: 291-315.

Berberian M. and King G.C.P., 1981. Toward a paleogeography and tectonic evolution of Iran, Can. J. Earth Sci., 18: 210-265.

Braud J., 1970. Les formations du Zagros dans la région de Kermanshah (Iran) et leurs rapports structuraux. C. R. Acad. Sci. Paris, 271: 1241-1244.

Braud J. and Bellon H., 1974 Données nouvelles sur le domaine métamorphique du Zagros (zone de Sanandaj–Sirjan) au niveau de Kermanshah-Hamadan (Iran): nature àge et interprétation des séries métamorphiques et des intrusions; évolution structurale. Rapport Univ. Paris-Sud, p. 1-20.

Burns L.E., 1985. The Border Ranges ultramafic and nafic complex, south-central Alaska: cumulate fractionates of island-arc volcanics. Can. J. Earth Sci., 22: 1020-1038.

Delaloye M. and Desmons J., 1980. Ophiolites and mélange terranes in Iran: A geochronological study and its paleotectonic implications. Tectonophysics, 68: 83-111.

Dercourt J., Zonenshian L.P., Ricou L.-E., Kazmin V.G., Le Pichon X., et al., 1986. Geological evolution of the Tethys Belt from the Atlantic to the Pamirs since the Lias. Tectonophysics, 123: 241-315.

Desmons J. and Beccaluva L., 1983. Mid-ocean ridge and island-arc affinities in ophiolites from Iran: palaeographic implications. Chem. Geol., 39: 39-63.

Dick H.J.B. and Bullen T., 1984. Chromian spinel as a petrogenetic indicator in abyssal and alpine-type peridotites and spatially associated lavas. Contrib. Mineral. Petrol., 86: 54-76.

Droop G.T.R., 1987. A general equation for estimating Fe^{3+} concentrations in ferromagnesian silicates and oxides from microprobe analyses, using stochiometric criteria. Mineral. Mag., 51: 431-435.

Frey F.A., 1969. Rare earth abundances in a high-temperature peridotite intrusion. Geochim. Cosmochim. Acta, 33: 1429-1447. doi: 10.1016/0016-7037(69)90183-5.

Fujimaki H., Tatsumoto M. and Aoki K., 1984. Partition coefficients of Hf, Zr, and REE between phenocrysts and groundmasses. J. Geophys. Res., 89, Supl. B1: 662-672.

Ghazi A.M. and Hassanipak A.A., 1999. Geochemistry of subalkaline and alkaline extrusives from the Kermanshah ophiolite, Zagros Suture Zone, western Iran: implications on Tethyan plate tectonics. J. Asian Earth Sci., 17: 319-332.

Glennie K.W., 2000. Cretaceous tectonic evolution of Arabia's eastern plate margin: a tale of two oceans, In: A.S. Alsharan and R.W. Scott (Eds.), Middle East models of Jurassic/Cretaceous carbonate systems. SEPM, Spec. Publ., 69: 9-20.

Golonka J., 2004. Plate tectonic evolution of the southern margin of Eurasia in the Mesozoic and Cenozoic. Tectonophysics, 381: 235-273.

Hébert R. and Laurent R., 1990. Mineral chemistry of the plutonic section of the Troodos ophiolite: New constraints for genesis of arc-related ophiolites, In: J. Malpas, E. Moores, A. Panayiotou and C. Xenophontos (Eds.), Proceed, Troodos Ophiolite Symposium. Geol. Survey Cyprus, p. 149-163.

Hickey R.L. and Frey A.F., 1982. Geochemical characteristics of boninite series volcanics: implications for their source. Geochim. Cosmochim. Acta, 46: 2099-2115.

Ishii T., Robinson P.T., Maekawa H. and Fiske R., 1992. Petrological studies of peridotites from diapiric serpentinite seamounts in the Izu-Ogasawara-Mariana forearc, Leg 125. In: P. Fryer, J.A. Pearce, L.B. Stokking et al. (Eds.), Proceed. O. D. P. Sci. Res., 125: 445-486.

Jackson M.L., 1958. Soil chemical analysis. Prentice-Hall, 498 pp.

Kinzler R.J., 1997. Melting of mantle peridotite at pressures approaching the spinel to garnet transition: application to mid-ocean ridge basalt petrogenesis. J. Geophys. Res., 102: 853-874.

Knipper A., Ricou L.E. and Dercourt J., 1986. Ophiolites as indicators of the geodynamic evolution of the Tethyan Ocean. Tectonophysics, 123: 213-240.

Koller F., Hoeck V., Meisel T., Ionescu C., Onuzi K. and Ghega D., 2006. Cumulates and gabbros in southern Albanian ophiolites: their bearing on regional tectonic setting. In: A.H.F. Robertson and D. Mountrakis (Eds.), Tectonic development of the Eastern Mediterranean Region. Geol. Soc. London Spec. Publ., 260: 267-299.

Kostopoulos D.K. and Murton B.J., 1992. Origin and distribution of components in boninite genesis: significance of the OIB component, In: L.M. Parson, B.J. Murton and P. Browning (Eds.), Ophiolites and their modern oceanic analogues. Geol. Soc. London Spec. Publ., 60: 133-154.

Lachance G.R. and Trail R.J., 1966. Practical solution to the matrix problem in X-ray analysis. Can. Spectrosc., 11: 43-48.

Leterrier J., 1985. Mineralogical geochemical and isotopic evolution of two Miocene mafic intrusions from the Zagros (Iran). Lithos, 18: 311-329.

Leturmy P. and Robin C., 2010a. Tectonic and stratigraphic evolution of Zagros and Makran during the Mesozoic-Cenozoic: Introduction. In: P. Leturmy and C. Robin (Eds.), Tectonic and stratigraphic evolution of Zagros and Makran during the Mesozoic-Cenozoic. Geol. Soc. London Spsc. Publ., 330: 1-4.

Leturmy P. and Robin C. (Eds.), 2010b. Tectonic and stratigraphic evolution of Zagros and Makran during the Mesozoic-Cenozoic. Geol. Soc. London Spec. Publ. 330, 360 pp.

Lippard S.J., Shelton A.W. and Gass I.G., 1986. The Ophiolite of Northern Oman. Geol. Soc. London Mem., 11, 178 pp.

McKenzie D. and O'Nions R.K., 1991. Partial melt distributions from inversion of rare Earth element concentrations. J. Petrol., 32: 1021-1091.

Meschede M., 1986. A method of discriminating between different types of mid-ocean ridge basalts and continental tholeiites with the Nb-Zr-Y diagram. Chem. Geol., 56: 207-218.

Morimoto N., 1989. Nomenclature of pyroxenes. Can. Mineral., 27: 143-156.

Pearce J.A., Barker P.F., Edwards S.J., Parkinson I.J. and Leat P.T., 2000. Geochemistry and tectonic significance of peridotites from the South Sandwich arc-basin system, South Atlantic. Contrib. Mineral. Petrol., 139: 36-53.

Pearce J.A. and Norry M.J., 1979. Petrogenetic implications of Ti, Zr, Y, and Nb variations in volcanic rocks. Contrib. Mineral. Petrol., 69: 33-47.

Pearce J.A., van der Laan S.R., Arculus R.J., Murton B.J., Ishii T., Parkinson I.J. and Peate D.W., 1992. Boninite and harzburgite from ODP Leg 125 (Bonin-Mariana forearc): a case study of magma genesis during the initial stages of subduction, In: P. Freyer, L.B. Stokking et al. (Eds.), Proceed. O. D. P., Sci. Res., 125: 623-659.

Pouchou J.L. and Pichoir F., 1985. PAP ø(pZ) procedure for improved quantitative microanalysis, In: J.T. Armstrong (Ed.), Microbeam analysis. San Francisco Press, San Francisco, p. 104-106.

Rampone E., Hofmann A.W., Piccardo G.B., Vannucci R., Bottazzi P. and Ottolini L., 1995. Petrology, mineral and isotope geochemistry of the External Liguride peridotites (Northern Apennines, Italy). J. Petrol., 36: 81-105.

Rampone E., Hofmann A.W. and Raczek I., 1998. Isotopic constraints within the Internal Liguride ophiolites (N. Italy): The lack of a genetic mantle-crust link. Earth Planet. Sci. Lett., 163: 175-189.

Ricou L.E., 1968. Une coupe à travers les séries à radiolarites des Monts Pichakum (Zagros, Iran). Bull. Soc. Géol. France, Sér. 7, T. 10: 478-485.

Ricou L.E., 1976. Evolution structurale des Zagrides. La région clef de Neyriz (Zagros iranien). Mem. Soc. Géol. France N.S., 55, 125, 140 pp.

Ricou L.E., Braud J. and Brunn J.H., 1977. Le Zagros. In: Livre à la mémoire de A.F de Lapparent, Soc. Géol. France, p. 33-52.

Robertson A.H.F., 1987. Upper Cretaceous Muti Formation: transition of a Mesozoic carbonate platform to a foreland basin in the Oman Mountains. Sedimentology, 34: 1123–1142.

Robertson A.H.F., 2007. Overview of tectonic settings related to the rifting and opening of Mesozoic ocean basins in the Eastern Tethys: Oman, Himalayas and Eastern Mediterranean regions. In: G. Karner, G. Manatschal and L. Pinheiro (Eds.), Imaging, mapping and modelling continental lithosphere extension and breakup. Geol. Soc. London Spec. Publ., 282: 325-389.

Ross K. and Elthon D. 1993. Cumulates from strongly depleted mid-ocean-ridge basalt. Nature, 365: 826-829.

Saccani E., Beccaluva L., Coltorti M. and Siena F., 2004. Petrogenesis and tectono-magmatic significance of the Albanide-Hellenide Subpelagonian ophiolites. Ofioliti, 29: 77-95.

Saccani E., Delavari M., Beccaluva L. and Amini S.A., 2010. Petrological and geochemical constraints on the origin of the Nehbandan ophiolitic complex (eastern Iran): Implication for the evolution of the Sistan Ocean. Lithos, doi:10.1016/j.lithos.2010.02.016.

Saccani E., Photiades A. and Beccaluva L., 2008. Petrogenesis and tectonic significance of IAT magma-types in the Hellenide ophiolites as deduced from the Rhodiani ophiolites (Pelagonian Zone, Greece). Lithos, 104: 71-84.

Sengor A.M.C., Altlner D., Cin A., Ustaomer T. and Hsu K.J., 1988. Origin and assembly of the Tethyside orogenic collage at the expense of Gondwana Land, In: M.G. Audley-Charles and A.E. Hallam (Eds.), Gondwana and Tethys. Geol. Soc. London Spec. Publ., 37: 119-181.

Shahidi M. and Nazari H., 1997. Geological map of Harsin, 1/100.000 scale. Geol. Survey Iran, Tehran.

Shervais J.W., 2001. Birth, death, and resurrection: The life cycle of suprasubduction zone ophiolites. G3- Geochem., Geophys., Geosyst., 2: 45 pp. (doi:10.1029/2000GC000080).

Sisson T.W. and Grove T.L., 1993. Experimental investigation of the role of H_2O in calc-alkaline differentiation and subduction zone magmatism. Contrib. Mineral. Petrol., 113: 143-166.

Stampfli G.M. and Borel G.D., 2002. A plate tectonic model for the Paleozoic and Mesozoic constrained by dynamic plate boundaries and restored synthetic oceanic isochrons. Earth Planet. Sci. Lett., 196: 17-33.

Stampfli G., Mosar J., Faure P., Pillevuit A. and Vannay J.-C., 2001. Permo-Mesozoic evolution of the western Tethys realm: the Neotethys East Mediterranean basin connection. In: P. Ziegler, W. Cacazza, A.H.F. Robertson and S. Crasquin-Soleau (Eds.), Peri-Tethyan rift/wrench basins and passive margins. Mem. Mus. Nat. Hist. Nat., Peri-Tethys Mem., 5: 51-108.

Stern R.J., Morris J., Bloomer S.H. and Hawkins J.W.J., 1991. The source of the subduction component in convergent margin magmas: trace element and radiogenic isotope evidence from Eocene boninites, Mariana forearc. Geochim. Cosmochim. Acta, 55: 1467-1481.

Stöcklin J., 1968. Structural history and tectonics of Iran: A review. Bull. Am. Ass. Petrol. Geol., 52: 1229-1258.

Stöcklin J., 1974. Possible Ancient continental margins in Iran. In: C.A. Burke and C.L. Drake (Eds.), The geology of continental margins. Springer-Verlag, New York, p. 873-887.

Stöcklin J., 1977. Structural correlation of the Alpine ranges between Iran and Central Asia. Mém. Soc. Géol. France, 8: 333-353.

Sun S.-S. and McDonough W.F., 1989. Chemical and isotopic-systematics of oceanic basalts: implications for mantle composition and processes. In: A.D. Saunders and M.J. Norry (Eds.), Magmatism in the ocean basins, Geol. Soc. London Spec. Publ., 42: 313-345.

Workman R.K. and Hart S.R., 2005. Major and trace element composition of the depleted MORB mantle (DMM). Earth Planet. Sci. Lett., 231: 53-72.

Wood D.A., 1980. The application of a Th-Hf-Ta diagram to problems of tectonomagmatic classification and to establishing the nature of crustal contamination of basaltic lavas of the British Tertiary volcanic province. Earth Planet. Sci. Lett., 50: 11-30.

Received, September 9, 2010
Accepted, December 2, 2010